

Fine-scale Segmentation and Spatiotemporal Variability of the 2010 Mw 8.8 Maule Aftershock Sequence Revealed by a Deep-Learning-Based Earthquake Catalog

Rodrigo Flores-Allende¹, Léonard Seydoux¹, Éric Beaucé^{2,3}, Luis Fabian Bonilla^{3,1},
Philippe Gueguen⁴ and Claudio Satriano¹

¹Université Paris Cité, Institut de physique du globe de Paris, UMR 7154, Paris, France

²Lamont-Doherty Earth Observatory, Columbia University, New York, NY, USA

³Université Gustave Eiffel, Champs-sur-Marne, Marne-la-Vallée, France

⁴ISTerre, Université Grenoble Alpes/CNRS/Univ. Savoie Mont-Blanc/IRD/Université Gustave Eiffel,
38000 Grenoble, France

Corresponding author: floresallende@ipgp.fr

Peer-review status:

This manuscript has been submitted to Journal of Geophysical Research: Solid Earth and is currently under review. It has not yet been formally accepted for publication. Subsequent versions of this manuscript may differ from this version.

1 **Fine-scale Segmentation and Spatiotemporal Variability**
2 **of the 2010 M_w 8.8 Maule Aftershock Sequence**
3 **Revealed by a Deep-Learning-Based Earthquake**
4 **Catalog**

5 **Rodrigo Flores-Allende¹, Léonard Seydoux¹, Éric Beaucé²,**
6 **Luis Fabian Bonilla^{3,1}, Philippe Gueguen⁴ and Claudio Satriano¹**

7 ¹Université Paris Cité, Institut de Physique du Globe de Paris, UMR 7154, Paris, France

8 ²Lamont-Doherty Earth Observatory, Columbia University, New York, NY, USA

9 ³Université Gustave Eiffel, Champs-sur-Marne, Marne-la-Vallée, France

10 ⁴ISTerre, Université Grenoble Alpes/CNRS/Univ. Savoie Mont-Blanc/IRD/Université Gustave Eiffel,
11 38000 Grenoble, France

12 **Key Points:**

- 13 • We build a dense catalog of 537,387 aftershocks of the 2010 M_w 8.8 Maule earthquake,
14 achieving a completeness magnitude of about M_w 1.8.
15 • Automated detection and relocation yield consistent magnitudes and improved loca-
16 tions across variable network coverage.
17 • Spatial b -values vary along strike, consistent with a weaker, fluid-rich northern plate
18 interface and a stronger southern megathrust segment.

Corresponding author: Rodrigo Flores-Allende, floresallende@ipgp.fr

Abstract

We re-examine the aftershock sequence of the M_w 8.8 Maule earthquake in south-central Chile to understand how seismicity, magnitude-frequency distribution, and fault structure vary along the rupture zone. Using the International Maule Aftershock Deployment (IMAD) dataset, we analyze ten months of continuous data from approximately 156 temporary stations and build a high-resolution aftershock catalog for the Maule rupture zone. We apply the BackProjection and Matched-Filtering (BPMF) workflow, which integrates a deep-learning phase picker with backprojection-based association, relative relocation, and template matching. We initially detect and relocate 130,575 earthquakes, then use a subset of high-quality events as templates to identify smaller earthquakes missed by initial detection. The final catalog contains 537,387 earthquakes, nearly 13 times more events than in previous studies, with a completeness magnitude of $\approx M_w$ 1.8 and magnitudes ranging from M_w 0.2 to M_w 6.2. A local magnitude (M_L) calibration provides a homogeneous magnitude scale across the network. The dense catalog reveals detailed seismotectonic features along the rupture. In the Pichilemu region, aftershocks delineate a shallow normal fault system with L-shaped geometry, whereas the Concepción area contains aseismic patches. Using the classical maximum likelihood and b -more-incomplete methods, we find that temporal b -values range between 1.2 and 1.6 early in the sequence and converge toward ≈ 1.0 . Meanwhile, b -values vary strongly along strike, with higher values in the north and lower values in the south. These contrasts are consistent with along-strike variations in effective stress and pore fluid pressure on the plate interface, in line with previous studies.

Plain Language Summary

After a large earthquake, the Earth continues to adjust through thousands of smaller earthquakes called aftershocks. Studying when and where these occur helps scientists understand how stress is released along the fault and improves estimates of future earthquake hazards. In this study, we revisit the aftershocks of the 2010 magnitude 8.8 Maule earthquake in south-central Chile. We analyze almost one year of data recorded by 156 temporary seismic stations. Using modern computational methods, including machine learning and template matching, we detect and locate many small earthquakes not identified before. The new catalog contains more than half a million events, about thirteen times more than in earlier studies. Aftershocks are not evenly distributed along the rupture zone. Near Pichilemu, earthquakes outline a shallow fault system, while deeper earthquakes occur within the oceanic plate sinking beneath South America. We also examine how the relative number of small and large earthquakes changes with time and location along the fault. These patterns provide clues about variations in stress, the presence of fluids, and rock strength. This study shows how modern analysis methods applied to existing seismic data can reveal new details about how large earthquakes rupture and how subduction zones evolve after major events.

1 Introduction

On February 27, 2010, a M_w 8.8 earthquake struck the Maule region in south-central Chile, causing significant loss of life and widespread damage (Salazar & McNutt, 2011). The rupture extended 500 km along the convergent margin between the Nazca and South American plates, spanning latitudes 33°S and 38.5°S (Figure 1a). This event ranks among the largest instrumentally recorded earthquakes worldwide and is the largest well-instrumented earthquake in Chile (e.g., Delouis et al., 2010; Madariaga et al., 2010; Moreno et al., 2010; Vigny et al., 2011; S. Ruiz et al., 2012; Hicks et al., 2014; S. Ruiz & Madariaga, 2018). Its rupture coincides with the mature seismic gap left by the M_w 8.3 earthquake of 1835 (see, e.g., Campos et al., 2002), and overlaps segments of previous major earthquakes, including the M_w 7.7 Talca (1928), M_w 8.1 Concepción (1960, e.g., Ojeda et al., 2020), and M_w 7.8 Arauco (1975) earthquakes. It also partially overlaps the M_w 9.5 Valdivia earthquake area

69 of 1960, the largest earthquake ever recorded (e.g., Madariaga et al., 2010; S. Ruiz et al.,
70 2012).

71 Earthquakes are typically followed by increased seismic activity known as aftershocks.
72 In subduction zones, megathrust earthquakes often produce particularly large and long-
73 lasting aftershock sequences. These events are generally smaller than the mainshock, with
74 the largest aftershock being on average about 1.2 magnitude units smaller (Báth, 1965), and
75 they can persist for weeks to years (Bilek & Lay, 2018). They result from stress perturbations
76 induced by the main rupture (Felzer et al., 2004), and their distribution across the rupture
77 zone often correlates with regions of high postseismic strain and substantial static stress
78 changes (Lange et al., 2012; Rietbrock et al., 2012). Shortly after the mainshock, two large
79 aftershocks of M_w 6.9 and M_w 7.0 struck the area of Pichilemu on March 11, 2010, at the
80 northern edge of the rupture zone (Farías et al., 2011; Lange et al., 2012; Rietbrock et al.,
81 2012; Ryder et al., 2012; J. A. Ruiz et al., 2014; Jara-Muñoz et al., 2022). These aftershocks
82 suggest a potential migration of seismicity or the reactivation of pre-existing fault systems
83 in the region.

84 Over the past decade, the International Maule Aftershock Deployment (IMAD) dataset
85 has been a key resource for studying the Maule aftershock sequence. Deployed within a few
86 weeks of the mainshock (Guéguen et al., 2011), this mobile seismic network covered the
87 entire rupture area (Figure 1a) and enabled the construction of some early earthquake cat-
88 alogs. For instance, Lange et al. (2012) applied classical Short-Term Average to Long-Term
89 Average (STA/LTA) automatic pickers to detect over 20,000 events in six months, while
90 Rietbrock et al. (2012) detected more than 30,000 events in just two months using the same
91 approach. These initial efforts provided a broad overview of the rupture segmentation, af-
92 tershock distribution, and fault reactivation. Using the catalog from Rietbrock et al. (2012),
93 Agurto et al. (2012) refined the locations of the largest aftershocks and performed regional
94 moment tensor (RMT) inversions to characterize spatio-temporal variations in seismic mo-
95 ment release. One of the main observations was the apparent lack of large aftershocks in
96 regions of highest coseismic slip (Agurto et al., 2012; Rietbrock et al., 2012). Although this
97 pattern appears to depend on the selected slip model, both studies found that only low-
98 magnitude seismicity was detected in these high-slip patches. This emphasizes the need for
99 accurate detection and location of small events to delineate and characterize the interaction
100 between seismic and aseismic patches. Furthermore, the contribution of these regions to the
101 total postseismic deformation budget remains unclear, and deeper intraslab contributions
102 to postseismic deformation may also be underestimated. Moreover, Neighbors et al. (2015)
103 estimated the high-frequency attenuation parameter kappa (κ), finding significant spatial
104 variability likely reflecting the combined effects of source, path, and site conditions, though
105 poorly correlated with surface geology. In parallel, Tassara et al. (2016) analyzed b -value
106 patterns in relation to afterslip and proposed contrasting mechanical domains along strike,
107 which they related to variations in fluid content and fault rheology. While both studies
108 provided valuable constraints, their resolution was limited by the number of events used, as
109 they considered only subsets of moderate-to-large magnitude aftershocks. In this study, we
110 build on these previous constraints using a much denser, magnitude-calibrated aftershock
111 catalog and a b -value estimator that is less sensitive to completeness, which allows us to
112 resolve the along-strike segmentation of the Maule rupture and to reassess the role of fluids
113 and effective normal stress in controlling aftershock behavior.

114 A clear understanding of aftershock patterns, afterslip distribution, and triggering
115 mechanisms is key to improving our knowledge of earthquake mechanics (Peng & Zhao,
116 2009; Yao et al., 2017; Minetto et al., 2022; Farge & Brodsky, 2025). Although often ne-
117 glected in stress-transfer models, small-magnitude earthquakes can collectively contribute
118 significantly to stress redistribution due to their high rate of occurrence and spatial clus-
119 tering. Marsan (2005) showed that small earthquakes can collectively contribute to stress
120 redistribution as much as larger events, emphasizing the importance of including micro-
121 seismicity in further analyses. For instance, S. Ruiz et al. (2017) used repeaters to reveal

122 aseismic processes before and after the 2017 M_w 6.9 Valparaiso earthquake. Their results
 123 suggest that small-scale seismicity may have triggered the mainshock and played an impor-
 124 tant role in the rupture dynamics. However, current studies mainly rely on large-magnitude
 125 aftershocks, as detecting smaller ones remains challenging. Seismic noise often hinders
 126 the detection of low-magnitude aftershocks, particularly when using traditional methods
 127 based on signal amplitude such as signal-to-noise ratio (SNR) or the previously mentioned
 128 STA/LTA trigger (see, e.g., Allen, 1982). Other factors, such as wave scattering and at-
 129 tenuation, further complicate the detection of small aftershocks, especially in regions with
 130 extensive rupture zones and sparse seismic networks as in the present study (Figure 1b).

131 Recent advances in deep-learning algorithms have significantly improved the quality
 132 of earthquake catalogs (Ross et al., 2019; Zhu & Beroza, 2019; Mousavi & Beroza, 2023).
 133 These methods are well suited for identifying low-magnitude events and provide more reliable
 134 locations, revealing fine-scale details of seismic sequences and fault structures (Beucé et
 135 al., 2019; Tan et al., 2021; Beucé et al., 2022; Mancini et al., 2022; Minetto et al., 2022).
 136 In this study, we use these techniques to reassess an old but valuable dataset recorded by
 137 the IMAD network (Beck et al., 2014). We build a high-resolution earthquake catalog of
 138 the Maule aftershock sequence and analyze how seismicity is distributed in space and time
 139 across the rupture zone. Our goal is to resolve how aftershock distribution, magnitude
 140 statistics, and fault structure vary along the Maule rupture zone, which has been only
 141 partially imaged in previous studies. We pursue three main objectives. First, we construct
 142 a dense and internally consistent catalog under strongly variable station coverage, combining
 143 automatic phase picking, backprojection-based association, and two relocation stages. Small
 144 earthquakes can then be used reliably to map fine-scale structures and stress heterogeneity.
 145 Second, we calibrate a regional local magnitude scale directly from Maule waveforms and
 146 reference moment magnitudes, and use it to obtain homogeneous M_L and M_w for all events.
 147 Third, we map spatial and temporal variations in the b -value and magnitude of completeness,
 148 and relate these patterns to the segmented plate interface and to the Pichilemu crustal fault
 149 system.

150 To achieve this, we follow the BPMF strategy of Beucé et al. (2024), which combines
 151 the deep-neural-network phase picker PhaseNet (Zhu & Beroza, 2019) with backprojection
 152 (Frank & Shapiro, 2014) for earthquake detection and initial location, followed by two re-
 153 location stages using NonLinLoc (Lomax, 2001; Lomax & Savvaidis, 2022) to build an initial
 154 catalog. We then apply template matching to these well-located events (Gibbons & Ringdal,
 155 2006; Frank & Shapiro, 2014; Beucé et al., 2018) to identify additional earthquakes that
 156 would otherwise be missed by conventional techniques, increasing the catalog completeness
 157 and extending the magnitude range (Minetto et al., 2022).

158 In the following sections, we first outline the tectonic context of south-central Chile,
 159 with a focus on the 2010 Maule earthquake and its aftershock sequence. We then describe
 160 the IMAD database and the BPMF method used for earthquake detection, association,
 161 and relocation, and we summarize the resulting catalog. Next, we present the magnitude
 162 calibration, derive homogeneous M_L and M_w , and perform a Gutenberg–Richter analysis,
 163 including a recent method for estimating the b -value that is less sensitive to time-dependent
 164 completeness. Finally, we analyze the spatiotemporal distribution of seismicity, compare
 165 the new catalog to previous ones, and discuss the implications for rupture segmentation and
 166 the Pichilemu fault system.

167 2 Geotectonic setting

168 The Maule segment of the south-central Chilean subduction zone (33° – 39° S) is a tec-
 169 tonic transition zone that accommodates oblique convergence between the Nazca and South
 170 American plates at approximately 66 mm/year (Haberland et al., 2009). This segment is
 171 bounded by the subducted Juan Fernández Ridge to the north and the Mocha Fracture
 172 Zone to the south, and marks a transition from a strongly coupled interface in central Chile

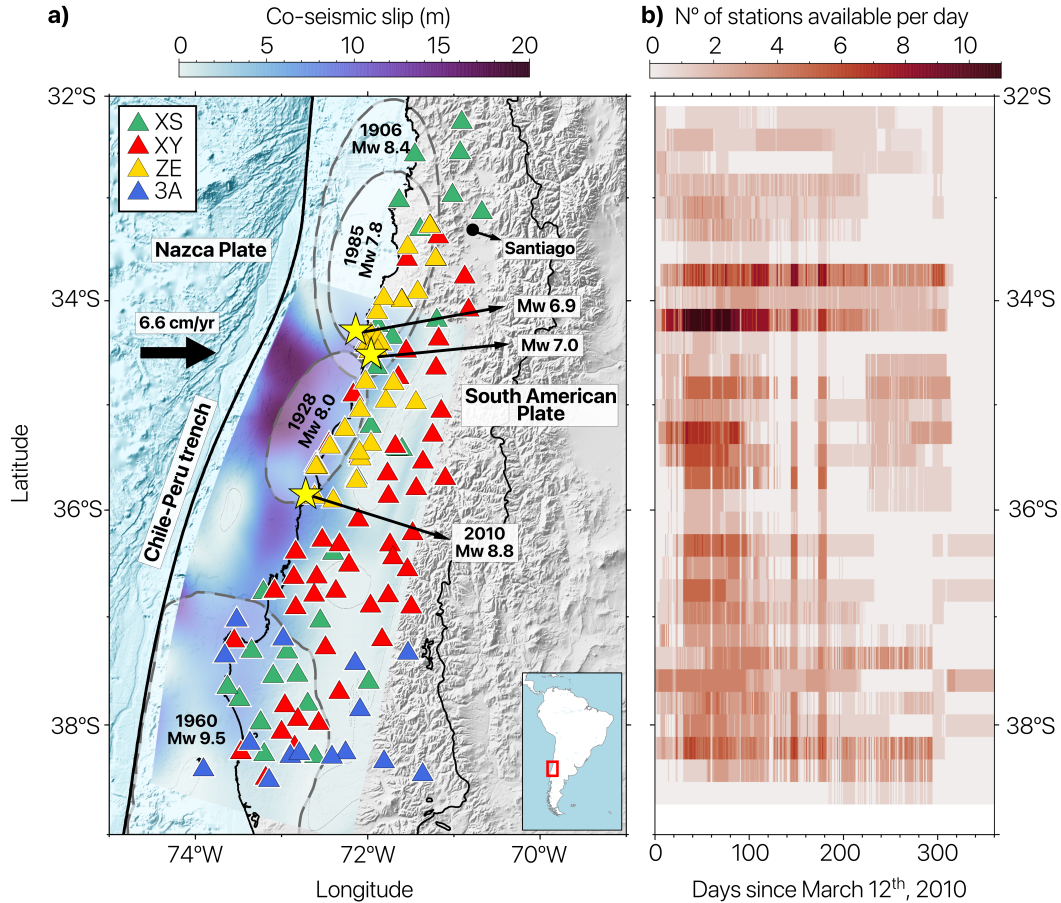


Figure 1. Study area and data coverage. (a) Seismic stations deployed in south-central Chile after the mainshock (triangles). Each color represents a network managed by different institutions: RESIF (XS in green, Vilotte et al., 2011), University of Florida (XY in red Steve Roecker & Ray Russo, 2010), GFZ (ZE in yellow), and University of Liverpool (3A in blue, Beck et al., 2014). The coseismic slip model presented by (Yue et al., 2014) is represented in background colors, with darker zones related to larger slip. The yellow stars mark the location of the M_w 8.8 mainshock on February 27, 2010, as well as the largest aftershocks in the Pichilemu zone ($34^{\circ}30'S$), with magnitudes M_w 6.9 and M_w 7.0. Historical rupture areas are depicted with gray ellipses. (b) Spatiotemporal availability of data. The color indicates the daily density of stations available every 0.2° of latitude.

173 to a more weakly coupled regime farther south (Moreno et al., 2010; Vigny et al., 2011).
 174 The segmentation is shaped by inherited lithospheric discontinuities, including the Lanalhue
 175 Fault Zone and terrane boundaries within a metamorphic Paleozoic basement intruded by
 176 Mesozoic granitoids (Hervé et al., 1987, 1988; Mpodozis & Ramos, 1990; Glodny et al.,
 177 2008; Aron et al., 2015). These crustal features influence upper-plate faulting, forearc up-
 178 lift, and mechanical coupling variations (Melnick et al., 2009). This geotectonically complex
 179 segment ruptured during the M_w 8.8 mainshock and is believed to have released the strain
 180 accumulated since 1835 (Campos et al., 2002; Ruegg et al., 2009). The rupture nucleated
 181 near 36.5°S and propagated bilaterally, producing two major slip patches. The northern
 182 patch reached peak slip values up to 20 m, overlapping the probable 1928 rupture zone and
 183 extending north toward the 1985 rupture border, whereas the southern patch reached ap-
 184 proximately 10 m of slip and overlapped the northern edge of the 1960 M_w 9.5 rupture zone
 185 (Figure 1a; Delouis et al., 2010; Lorito et al., 2011; Pollitz et al., 2011; S. Ruiz et al., 2012;
 186 Yue et al., 2014). Despite its magnitude, the Maule earthquake may not have fully released
 187 all the accumulated stress (Madariaga et al., 2010; Moreno et al., 2010), underscoring the
 188 role of margin segmentation and structural inheritance in governing rupture propagation
 189 and seismic potential. Along-strike changes in plate coupling, coseismic slip, and forearc
 190 structure suggest a segmented behavior of the Maule rupture, with contrasting conditions
 191 between the northern, central, and southern segments (Moreno et al., 2010; J. A. Ruiz et
 192 al., 2014; Tassara et al., 2016). The crustal Pichilemu fault system accommodates part of
 193 the shallow extension above the plate interface and hosts intense upper-crustal seismicity
 194 during the aftershock phase (Farías et al., 2011; Rietbrock et al., 2012). These contrasts
 195 in structure and kinematics provide a natural framework to interpret spatial variations in
 196 frequency–magnitude statistics and b -values, and to relate them to differences in coupling,
 197 stress conditions, and fluid content along the margin.

198 3 Data and Preprocessing

199 We retrieve one year of seismic data from the IMAD dataset, which corresponds to a
 200 postseismic mobile network operated by France, the United States, Germany, the United
 201 Kingdom, and collaborating partners, covering the period from March 2010 to March 2011
 202 (see, e.g., Beck et al., 2014). This seismic array includes nearly 156 instruments equipped
 203 with accelerometers, short-period seismometers, and broadband seismometers (Figure 1a).
 204 Stations were deployed across the entire rupture area (Figure 1a), though not all operated
 205 simultaneously or for the same duration (Figure 1b). Also, external conditions cause fluc-
 206 tuations in station availability over time, making the dataset non-uniform (Lange et al.,
 207 2012). During certain periods, fewer than 20 stations are operational, while at most, nearly
 208 120 stations are simultaneously active.

209 To mitigate this variability, we exclude stations and traces with substantial data gaps.
 210 In regions with multiple stations within a 500 m radius, we select one station to avoid
 211 redundancy. Finally, we focus on periods with consistent availability of at least five stations,
 212 defined as the lowest threshold providing sufficient spatial and temporal coverage. This
 213 minimum threshold does not vary across the study area or over time, although the specific
 214 station combinations may change depending on the variable network configuration. The
 215 sequential steps of the workflow are illustrated in Figure 2, with further details provided in
 216 the subsequent sections.

217 We bandpass-filter the continuous data between 1 and 20 Hz to discard low-frequency
 218 noise. We select this frequency range from an initial visual inspection of the data, which
 219 show energy concentrations mainly above 1 Hz. This approach is consistent with the param-
 220 eters applied by Cabrera et al. (2021) in a similar tectonic context. Continuous waveforms
 221 are processed at the native sampling rate of each station and used for detection, relocation,
 222 and magnitude estimation. In addition, we ensure the inclusion of only stations with min-
 223 imal data gaps and consistent operational records. We include data segments if they meet
 224 two key criteria: (1) a minimum total data availability of 75% of the station’s expected

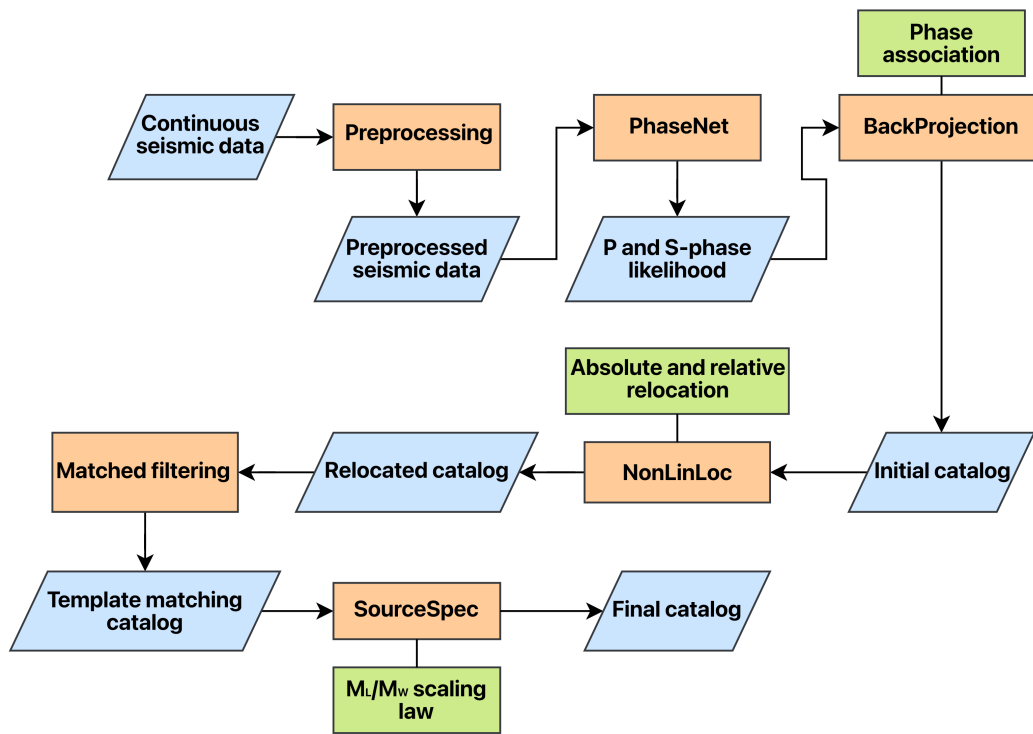


Figure 2. Earthquake catalog workflow. Blue boxes represent data (inputs or outputs), orange boxes indicate processing steps, and green boxes denote major stages of the workflow. The diagram summarizes the sequence of steps used to detect events, relocate earthquakes, and estimate magnitudes used to build the final catalog.

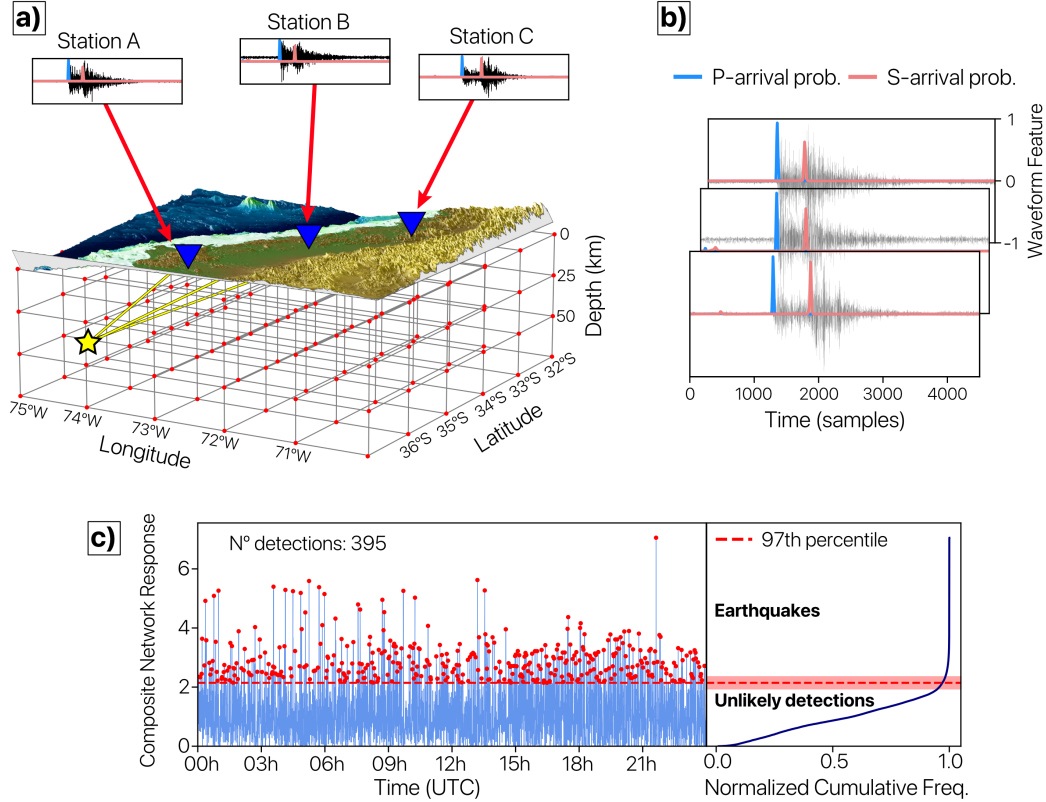


Figure 3. Earthquake detection and initial location. (a) Illustration of the grid with tested source points. The yellow star indicates the true earthquake location, with corresponding signals recorded at the seismic stations. (b) Example seismic record with the P and S likelihoods obtained using PhaseNet (Zhu & Beroza, 2019), shown in blue and orange, respectively. (c) Composite network response obtained by shifting and stacking the waveform features for each component and station over time (Beaucé et al., 2024). The dashed red line shows the 97th percentile detection threshold, with red points indicating events interpreted as localized sources.

225 operational period, ensuring sufficient temporal coverage despite potential gaps, and (2) in-
 226 dividual contiguous chunks with a duration of at least 600s, excluding excessively short
 227 fragments unsuitable for the analysis.

228 This workflow is based on the BPFM algorithm (Beaucé et al., 2024) whose outputs
 229 are post-processed with the NonLinLoc, Source-Specific Station Term (SSST) correction and
 230 waveform coherence relocation algorithm (Lomax & Savvaidis, 2022) to enhance earthquake
 231 locations, and SourceSpec to estimate the moment magnitudes (Satriano, 2021). These
 232 tools complement the original framework and were included to increase the robustness of
 233 the results.

234 4 Earthquake Catalog

235 4.1 Detection and Phase Association

236 To detect and locate the initial earthquakes, we build a 3D spatial grid of potential
 237 point sources (Figure 3a). The grid covers the full extent of the rupture area, with a

horizontal spacing of 0.03° in both latitude and longitude, a vertical spacing of 0.5 km, and a maximum depth of 100 km. This parameterization is consistent with the effective resolution of the 3D velocity model used in this study for south-central Chile (Figure S1 in the Supporting Information; Potin et al., 2025) and provides a practical compromise between spatial resolution and computational cost.

We compute the P- and S-wave travel times (moveouts) τ_{sk}^ϕ from each grid point k to station s for the seismic phase $\phi \in \{P, S\}$ by solving the eikonal equation (White et al., 2020).

We then use the deep-learning automatic phase picking algorithm PhaseNet (Zhu & Beroza, 2019) to estimate the probabilities $\nu_{s\phi}(t)$ of P - and S -wave arrivals in continuous seismic data (as illustrated in Figure 3b and Figure S2 in Supporting Information). Next, we shift $\nu_{s\phi}(t)$ according to the computed moveouts and stack the waveform features to identify the most likely source location. This serves as an efficient seismic phase association mechanism (see also Figure 3c). This stacked response follows the beamforming approach of Frank and Shapiro (2014) and is defined as:

$$b_k(t) = \sum_{s \in \mathcal{S}_k} \sum_{\phi \in \{P, S\}} \nu_{s\phi}(t + \tau_{sk}^\phi) \quad (1)$$

Coherent seismic signals produce higher values of $b_k(t)$ when aligned with a likely source k , whereas incoherent noise contributions do not sum constructively. The set of seismic stations \mathcal{S}_k includes only the ten closest stations to the source k to enhance source-to-station sensitivity. The final source location is determined by identifying the maximum value of the composite network response (CNR) defined as the beamforming maximum over time $\mathcal{B}(t) = \max_k b_k(t)$.

The CNR allows the detection and location of earthquakes with increased sensitivity and precision (Beaucé et al., 2019, 2022, 2024). It provides an initial estimate of the event location by identifying the time at which the beam power reaches its peak. However, the accuracy of this location strongly depends on the grid resolution and the velocity model. A finer grid, with more potential source points k , improves spatial precision but drastically increases computational cost. A key challenge in this process is to distinguish between beams corresponding to real earthquakes and those resulting from noise, unlikely signals, or artifacts. Finally, given the large study area and the heterogeneous station coverage, the stacked signal response varies over time, making the choice of a detection threshold non-trivial. To address this, we implement a dynamic threshold approach based on the daily cumulative distribution function (CDF) of the CNR. Assuming that most low-amplitude beams do not correspond to real events, we define the threshold at the point of maximum curvature (“knee”) of the empirical CDF (Figure 3c). However, in cases where the knee is not well-defined, the uncertainty in event detection may increase. To maintain a conservative yet effective detection criterion, we set the threshold at the 97th percentile of the beam power distribution. We also note that values between the 95th and 99th percentiles can effectively distinguish potential seismic signals while reducing the likelihood of false detections. This adaptive approach ensures that the detection threshold dynamically adjusts to the empirical characteristics of the dataset, optimizing the balance between sensitivity and reliability.

Applying this approach, we detect 130,575 earthquakes during the study period. Each event has P- and S-wave picks from at least five stations, resulting in nearly six million valid picks (about 2.7 million P and 3.1 million S arrivals). Backprojection provides initial locations on the 3D grid described above, and the computations are accelerated on GPUs to keep runtimes practical for this large dataset.

4.2 Event relocation

To improve location accuracy, we relocate all detections with the NonLinLoc-SSST-Coherence algorithm (Lomax, 2001; Lomax et al., 2009; Lomax & Savvaidis, 2022). Non-

LinLoc uses the P - and S -wave picks previously identified by PhaseNet to perform a grid search and sample the likelihood of hypocenter locations in the regional 3D V_P/V_S velocity model (Figure S3 in the Supporting Information; Potin et al., 2025). For each of the 130,575 events, it returns an absolute hypocenter and an uncertainty ellipsoid, which form the basis for the subsequent stages.

Then, we apply Source-Specific Station Term (SSST) corrections, which iteratively refine travel-time estimates by minimizing residuals between observed and predicted seismic phase arrivals (Figure S4). This approach accounts for spatial velocity variations, producing smoother station-specific travel-time corrections that adapt to regional heterogeneities, resulting in more precise earthquake locations. P - and S -phase residuals show distinct spatial patterns across the network (see Figure S4 in the Supporting Information). P -wave arrivals are slightly delayed near 35-36°S, consistent with locally overestimated P -wave velocities, whereas S -wave arrivals are systematically earlier across most stations, consistent with underestimated shear-wave velocities in the adopted 3D model (Potin et al., 2025). Such coherent residuals arise when velocity heterogeneities are spatially correlated, so that path-dependent prediction errors do not average out and instead produce persistent, station-dependent biases (Myers et al., 2015). Given the predominantly north-south network geometry, absolute locations may therefore retain a small systematic location bias, which is partly mitigated by the coherence relocation.

Finally, we apply a relative relocation method based on waveform coherence (Lomax & Savvaidis, 2022). Conceptually, it is similar to other techniques such as HypoDD (Waldhauser, 2001) or GrowClust (Trugman & Shearer, 2017), but without relying on differential travel times. High waveform coherence, quantified by the maximum cross-correlation, suggests that close events originate from nearby sources. We stack the location PDFs of highly correlated events and relocate them within their shared probability region. This approach enhances location accuracy, even in regions with sparse station coverage and limited datasets, such as in our case.

The result of this three-step workflow on the catalog is summarized in Figure 4. To allow a direct comparison of how earthquake locations evolve through the workflow, we plot only those events that successfully passed all relocation stages. Out of the initial 130,575 earthquakes, 5,704 events retain their first location, 78,569 events are updated only by the SSST correction, and 46,302 events undergo the full coherence relocation. The median horizontal semi-major axis is 1.2 km, the median semi-minor axis is 0.5 km, and the median vertical uncertainty is 1.6 km across all events. For the maps in Figure 4 we further restrict the plotting to the 42,459 relocated earthquakes with a horizontal uncertainty smaller than 10 km. Panels a–b and a’–b’ show initial and final locations color-coded by depth, while panels c and c’ show the $\log_{10}(V_{\text{ini}}/V_{\text{fin}})$ uncertainty reduction ratio. In the outer-rise zone (dashed red ellipse, Figure 4a–c), locations change only slightly and uncertainty reduction is limited, reflecting poor offshore constraints from the available network geometry and pick quality. In contrast, within the Pichilemu fault system (solid red box, Figure 4a’–c’), the relocation sharpens the seismicity distribution into more compact clusters that better align with mapped structures, with markedly higher uncertainty reduction driven by waveform coherence among similar events.

4.3 Template matching

Template matching is a technique used to identify low SNR earthquakes by cross-correlating continuous seismic data with existing template waveforms (Anstey, 1964; Gibbons & Ringdal, 2006; Shelly et al., 2007; Frank & Shapiro, 2014; Skoumal et al., 2014; Beaucé et al., 2018; Cabrera et al., 2021; Beaucé et al., 2022; Minetto et al., 2022). This process quantifies the similarity between seismic waveforms, triggering a new detection when the correlation is sufficiently high (Figure S5). We define as templates a subset of earthquakes whose largest horizontal semi-major axis of the location error ellipse is smaller than

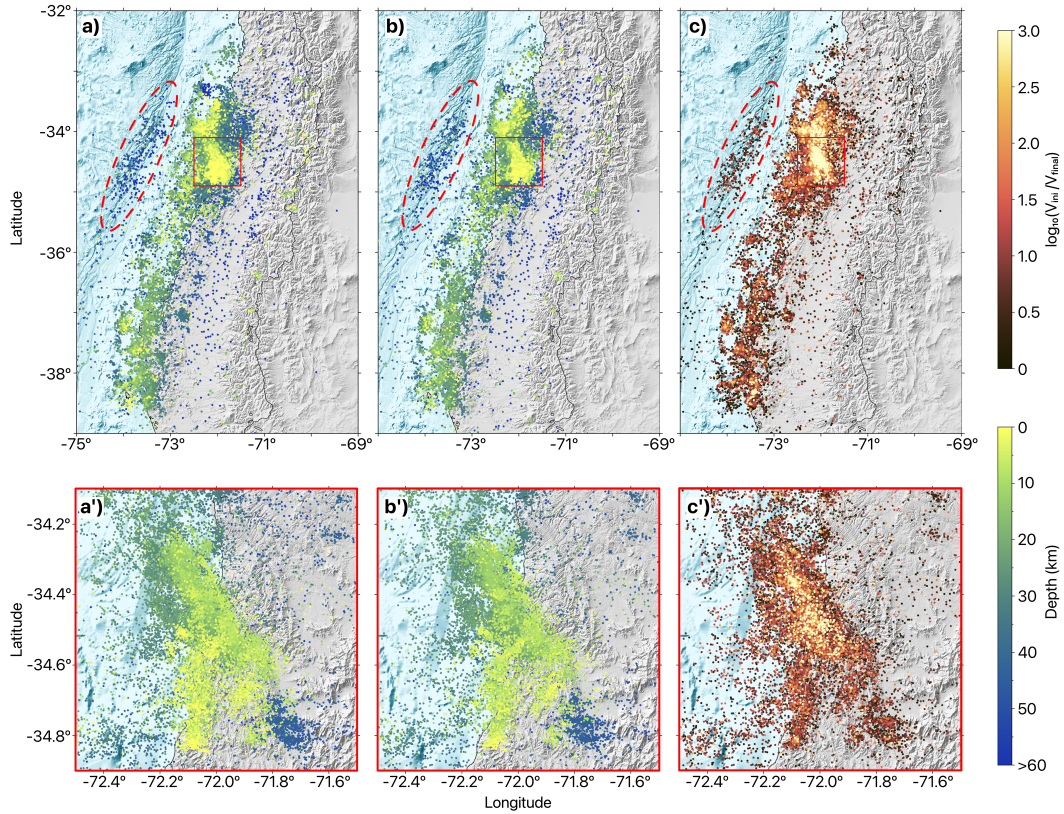


Figure 4. Improved earthquake locations. The top row shows the full study area, while the bottom row presents a close-up of the Pichilemu fault system (red box). The dashed red ellipse outlines the outer-rise seismicity zone. **(a, a')** Initial earthquake hypocenters from the first-stage NonLinLoc locations, color-coded by depth (color scale saturated above 60 km). **(b, b')** Final event locations after the coherence-based improvement in NonLinLoc, using the same depth scale. **(c, c')** \log_{10} ratio of the initial to final location uncertainty ellipsoid volume, $V_{\text{ini}}/V_{\text{fin}}$, plotted at the final event locations. This metric quantifies the reduction in location uncertainty achieved by the relocation procedure. Higher values (brighter colors) indicate stronger uncertainty reduction, whereas values near zero (darker colors) indicate limited improvement over the initial solution.

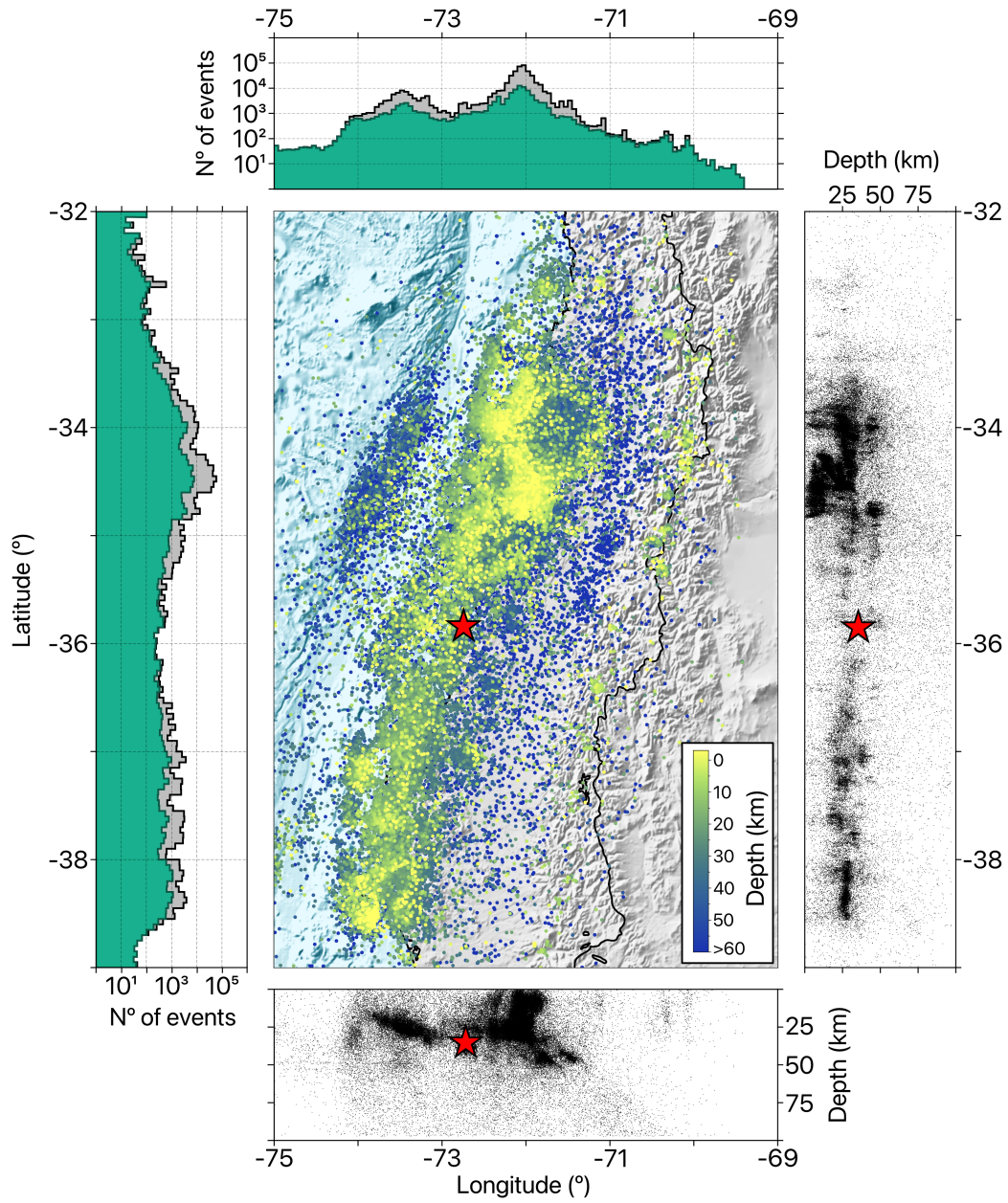


Figure 5. Spatial distribution of the aftershocks in the study area. The central panel shows the final locations of the full catalog, color-coded by depth, together with the M_w 8.8 mainshock marked by a red star. The top and left panels show the number of earthquakes as a function of longitude and latitude, respectively, with the event-count axes plotted on a logarithmic scale. The green histograms represent the initial catalog, while the gray histograms represent the final catalog after template matching. The right and bottom panels display stacked depth profiles of the earthquake catalog. The bottom panel illustrates the subduction geometry across different longitudes, while the right panel shows the concentration of seismicity with latitude as a function of depth. The red star marks the location of the mainshock.

337 2 km. To avoid redundancy, we group highly correlated events and keep, for each group, the
 338 one with the smallest combined horizontal and vertical uncertainty. Each template consists
 339 of a 10 s window around the picked P wave on the vertical component and the picked S
 340 wave on the horizontal components.

341 We finally cross-correlate the continuous data with the templates to identify coherent
 342 signals. New detections are recorded when the cross-correlation coefficient exceeds a time-
 343 dependent threshold, calculated as 8 times the root mean square (RMS) of each 30 min
 344 segment, which is consistent with conservative thresholds used in previous template match-
 345 ing studies (e.g., Shelly et al., 2007; Ross et al., 2019; Beaucé et al., 2022). We require
 346 a minimum of three available stations and six channels to trigger a new detection, based
 347 on the network-averaged cross-correlation coefficient, and limit the search to a maximum
 348 of ten stations per template, selected based on proximity, to optimize performance in large
 349 seismic networks. For each new detection, we assign the hypocenter of its parent template.
 350 Template detections therefore densify the catalog and extend the magnitude range, but they
 351 do not improve the spatial resolution beyond that of the template set. To ensure that the
 352 catalog contains only unique events, we apply a combination of geographic, temporal and
 353 similarity-based filters. Events that occur within 4 s and within 10 km of each other are
 354 grouped as potential duplicates. Within each group we retain only one event, preferring the
 355 detection with the highest template correlation and, when correlations are similar, the one
 356 with the smallest location uncertainty. This procedure removes redundant detections while
 357 keeping the most reliable representative in each cluster.

358 From the relocation process, we identify 55,328 well-located earthquakes with location
 359 uncertainties below 2 km, which serve as templates. To prevent redundant detections caused
 360 by highly similar events, we perform a waveform cross-correlation analysis, removing du-
 361 plicates and retaining 37,990 unique templates. Applying template matching with these
 362 events results in the detection of 406,812 new earthquakes, increasing the number of events
 363 by a factor of 10.7 compared to the starting subset of templates. We assign the locations of
 364 these newly detected events to their corresponding parent template, assuming that family
 365 members rupture closely spaced sources around the template hypocenter. As shown in the
 366 histograms in Figure 5 (top and left panels), the green area represents the initial catalog,
 367 while the gray area corresponds to the final catalog after template matching, with bin sizes
 368 of 0.1° . Most seismicity is concentrated in the Pichilemu area ($34\text{--}35^\circ\text{S}$, $71.5\text{--}72.5^\circ\text{W}$),
 369 where we identify the highest density of events both before and after template matching.
 370 In practice, the spatial resolution of the catalog is determined by the 130,575 events ini-
 371 tially detected and relocated with NonLinLoc-SSST-Coherence, while template detections
 372 primarily extend the temporal sampling and magnitude range within the same rupture area.

373 4.4 Magnitude Estimation

374 To complete our earthquake catalog, we compute the moment magnitude (M_w) using
 375 the Hanks and Kanamori (1979) equation (see also Table S1 in Supporting Information):

$$M_w = \frac{2}{3}(\log_{10} M_0 - 9.1), \quad (2)$$

376 where M_0 is the seismic moment, derived from the stacking and fitting of the Brune model
 377 (Brune, 1970) to the S -wave displacement spectra recorded by the seismic network (Satriano,
 378 2021). We use S -wave signal windows starting 1 s before the S pick, with an event-station
 379 distance-dependent duration (minimum 10 s). We estimate the noise window from pre-event
 380 data ending 1 s before the P pick, using the same window duration (see also Table S1 in
 381 the Supporting Information). Brune’s model fitting is performed over 0.01–50 Hz using
 382 frequency-dependent weights derived from the spectral SNR, so that the low-frequency rise,
 383 often dominated by noise, receives almost zero weight and does not bias the fit.

384 The obtained M_0 values are then integrated into Equation 2 to compute M_w . Mo-
 385 ment magnitude is advantageous for representing earthquake size, as it does not saturate

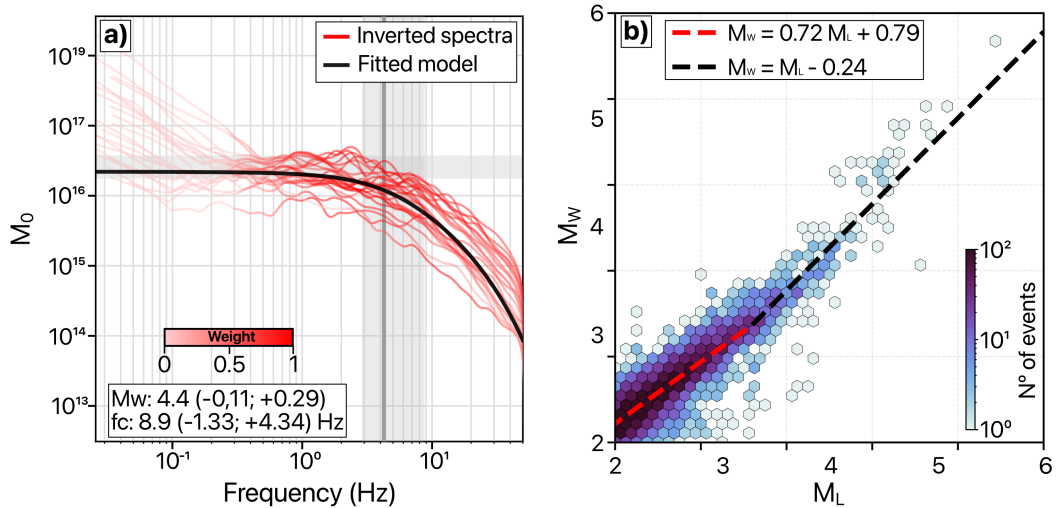


Figure 6. Moment magnitude estimation and M_L calibration. (a) Example displacement spectra used to estimate the seismic moment M_0 . Red lines show the displacement spectra recorded at different stations for this event, with Brune’s model fitted to the stacked spectra (black line). Color intensity encodes the frequency-dependent weights derived from the corresponding noise spectra, down-weighting low signal-to-noise bands, typically at low frequencies. The vertical dark gray rectangle indicates the estimated corner frequency. Additional examples are shown in Figures S6–S9. (b) Empirical M_L - M_w scaling derived from nearly 7,000 earthquakes in our catalog, represented by well-constrained spectral fits, showing a bilinear regression with a breakpoint at $M_L = 3.6$.

386 at large magnitudes and remains reliable across a broad range of seismic events. However,
 387 estimating M_w for small earthquakes is challenging because the associated ground motion is
 388 often masked by background noise. Accurate estimation of M_w for these small-scale events
 389 relies heavily on the sensitivity of instruments and the density of near-field stations. For
 390 the smallest earthquakes, the sampling rate also becomes a limiting factor, because their
 391 expected corner frequencies approach or exceed the usable frequency band. In practice, we
 392 can only estimate M_0 and M_w reliably for events whose spectra are well sampled around
 393 the corner frequency.

394 Therefore, for smaller events or when data quality is insufficient, we estimate M_w by
 395 scaling from local magnitudes (M_L) to homogenize our catalog (Deichmann, 2017). To
 396 obtain M_L values for our earthquakes, we first recalibrate the distance-dependent attenua-
 397 tion term in the classical Richter (1935) relation for south-central Chile. This calibration is
 398 performed with a joint inversion of amplitude and distance, following the procedure and recom-
 399 mendations of Bormann (2012) and similar regional studies (e.g., Langston et al., 1998;
 400 Y.-M. Wu et al., 2005; Condori et al., 2017).

401 We use 7,119 events with reliable M_w values computed with SourceSpec (Satriano,
 402 2021) as reference magnitudes. These earthquakes span from $M_w \approx 2.0$ to 6.5 and cover
 403 hypocentral distances between 10 and 250 km. The inversion includes a soft constraint that
 404 keeps the estimated M_L close to M_w for events with small M_w uncertainties, so that the re-
 405 sulting local-magnitude scale remains consistent with the moment-magnitude reference. For
 406 each event–station pair, we extract the horizontal waveforms, simulate a Wood–Anderson
 407 seismograph, and measure the zero-to-peak displacement amplitude, which we associate
 408 with the corresponding reference M_w and hypocentral distance.

409 We describe the distance dependence with a two-term attenuation function that com-
 410 bines geometric spreading and anelastic decay. For each event i and station j we assume

$$\log_{10} A_{ij} = M_{L,i} - a \log_{10} \left(\frac{R_{ij}}{R_{\text{ref}}} \right) - b (R_{ij} - R_{\text{ref}}) - S_j, \quad (3)$$

411 where each amplitude observation A_{ij} is related to the unknown local magnitude $M_{L,i}$, the
 412 hypocentral distance R_{ij} , and a station correction S_j .

413 We solve for all parameters simultaneously using a least squares inversion. The coef-
 414 ficients a and b control the average decay of amplitudes with distance, while S_j represents
 415 a static correction that accounts for local site and instrument effects. To avoid trade-offs
 416 between the S_j values and the overall magnitude level, we enforce that the network mean
 417 of the station terms is zero, which defines a unique reference for the entire network.

418 We adopt a reference distance of $R_{\text{ref}} = 100$ km, which is commonly used in regional
 419 M_L calibrations (Richter, 1935). This value also lies near the center of our sampled distance
 420 range. The first term, a , mainly reflects the effective wavefront geometry and average crustal
 421 structure, while the second term, b , represents moderate anelastic attenuation. The station
 422 terms S_j describe local deviations from the mean amplitude field and are applied directly
 423 in the final magnitude equation (Eq. 5) to correct for site-specific amplification.

424 This approach yields a stable and physically consistent calibration of the local mag-
 425 nitude scale, so we can compute homogeneous M_L values across the network and derive
 426 consistent M_w estimates for smaller events.

427 The preferred solution of this inversion corresponds to,

$$a = 1.4209, \quad b = 0.000736 \text{ km}^{-1}, \quad (4)$$

428 and provides a good fit to the amplitude data. The fit has a mean absolute error of 0.19
 429 magnitude units, a root mean square error of 0.25, and a negligible mean bias in $\log_{10} A$
 430 residuals. This root mean square error corresponds to a standard deviation of about 0.25
 431 magnitude units in the residuals. At the event level, the anchored M_L values differ from
 432 M_w^{ref} with a mean absolute difference of 0.20, a root mean square error of 0.30, and a
 433 small positive bias of 0.09 in magnitude. These values indicate that the calibrated M_L scale
 434 is internally consistent with the observed amplitudes and externally consistent with the
 435 reference M_w . Once the inversion parameters are fixed, we use the following M_L equation
 436 in this study,

$$M_L = \log_{10} A_{WA} + 1.4209 \log_{10} \left(\frac{R_{\text{hyp}}}{100} \right) + 0.000736 (R_{\text{hyp}} - 100) + S_j, \quad (5)$$

437 where A_{WA} is the Wood–Anderson zero to peak displacement amplitude and R_{hyp} is the
 438 hypocentral distance in km.

439 Figure 6a illustrates the stacking of displacement spectra from multiple stations for
 440 an earthquake (see also Figures S6-S9 in the Supporting Information), which we use to
 441 estimate the seismic moment M_0 and derive M_w (Equation 2). Based on this information, we
 442 calibrate the local magnitude M_L to estimate M_w for the entire catalog using the following
 443 relationship (Equation 6):

$$M_w = \begin{cases} 0.72M_L + 0.79 & \text{if } M_L \leq 3.6, \\ M_L - 0.24 & \text{otherwise.} \end{cases} \quad (6)$$

444 These two branches reflect the empirical observation that the scaling between M_L and M_w
 445 deviates from linearity at low magnitudes (Figure 6b). Consistent with Deichmann (2017),
 446 small earthquakes tend to follow a steeper scaling (approximately 1.5:1), while moderate to
 447 large events approach a 1:1 relationship. We fit a maximum likelihood bilinear regression

448 and obtain a breakpoint at $M_L = 3.6$, although the precise breakpoint may vary across
 449 datasets. A bootstrap analysis based on 1,000 resamples indicates a 95% confidence interval
 450 between $M_L = 3.41$ and $M_L = 3.86$. Allowing the breakpoint to change within this range
 451 produces only minor changes in the estimated M_w values. The median variation is $\delta M_w =$
 452 0.003 (16th–84th percentile range: $\delta M_w = 0.001$ – 0.011), and 99.6% of events differ by less
 453 than $\delta M_w = 0.1$.

454 This approach homogenizes the magnitude scale across the catalog and produces M_w
 455 values ranging from 0.22 to 6.20. The resulting catalog has an average magnitude of 2.08
 456 and a completeness magnitude (M_c) of approximately 1.8. The majority of events cluster at
 457 lower magnitudes, with the first quartile at $M_w 1.83$, the median at $M_w 2.01$, and the third
 458 quartile at $M_w 2.25$. Approximately 90% of the events have magnitudes below $M_w 2.61$.
 459 Periodic spikes in event counts likely correspond to secondary aftershocks triggered by the
 460 largest aftershock. Most events fall within the $M_w 2$ – 3 range, while the larger magnitudes,
 461 up to $M_w 6$, are concentrated in the Pichilemu region, which also hosted the two largest
 462 aftershocks ($M_w 6.9$ and 7.0). However, the seismic network became fully operational only
 463 a few days after these two events, so they are not included in this catalog.

464 4.5 Frequency–Magnitude Characteristics and b -Value Estimation

465 We analyze the frequency–magnitude distribution across our study area, using the
 466 widely applied Gutenberg–Richter relationship (Gutenberg & Richter, 1944)

$$\log_{10} N(\geq M) = a - bM, \quad (7)$$

467 where $N(\geq M)$ represents the cumulative number of earthquakes with magnitudes greater
 468 than or equal to M . The constant a estimates the seismic activity level in the region, while
 469 b describes the relative proportion of high- to low-magnitude earthquakes and typically
 470 takes values near 1. This analysis also requires an estimate of the catalog’s magnitude of
 471 completeness M_c , defined as the minimum magnitude above which the catalog is considered
 472 complete. However, this analysis may be biased in cases of periodically low availability of
 473 stations or spatiotemporal incompleteness of the catalog (Geffers et al., 2022).

474 To address the challenges in estimating the b -value, we apply the b -more-incomplete
 475 method (Lippiello & Petrillo, 2024), which builds upon the b -positive method (van der Elst,
 476 2021) but improves accuracy by artificially increasing the level of incompleteness in the
 477 catalog before estimating b . While the b -positive method calculates b from positive mag-
 478 nitude differences between successive earthquakes, the b -more-incomplete method enhances
 479 robustness by filtering out smaller events that could introduce bias due to short-term after-
 480 shock incompleteness (STAI). It reduces sensitivity to time-dependent changes in detection
 481 threshold and to biases introduced by overlapping coda waves and sparse network coverage.
 482 In practice, the b -more-incomplete method progressively removes the smallest events until
 483 the estimated b -value stabilizes with respect to further changes in the magnitude threshold.
 484 This results in an effective b -value that is controlled by the more reliably detected part of
 485 the catalog, without relying on the magnitude of completeness.

486 The temporal variation in the number of available IMAD stations since March 12, 2010,
 487 is shown in Figure 7a, together with the daily median location uncertainties of earthquakes.
 488 Station availability fluctuates strongly, especially after the first three months, when a grad-
 489 ual decline is observed, with only brief week-long recoveries. Toward the end of the period,
 490 the number of available stations stabilizes at approximately 15. These fluctuations directly
 491 affect earthquake detection and location accuracy, and periods of reduced station coverage
 492 coincide with increased location uncertainties (Figure 7a). This effect is also evident in
 493 Figure 7b, where regions with dense station coverage (Figure 1b), such as Pichilemu (34°
 494 to 35° S), exhibit a higher density of events. Conversely, regions with lower station avail-
 495 ability show detection gaps, particularly between 35° to 37° S after about 100 days from
 496 the start of the study period. Larger magnitude events are predominantly concentrated at

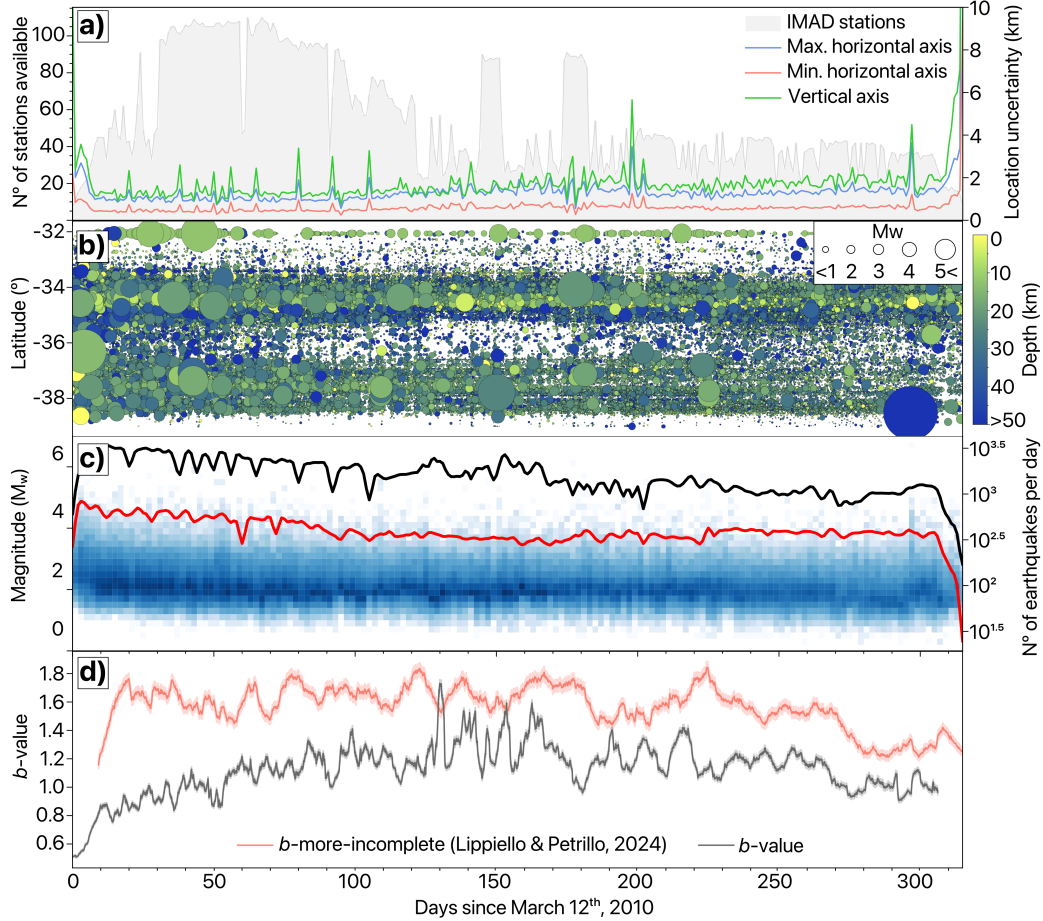


Figure 7. Temporal variations in (a) station availability (gray area) and earthquake location uncertainties (colored lines for maximum axis, minimum axis, and depth), (b) the spatial distribution in latitude, where circle size represents event magnitude and color indicates depth, (c) the magnitude variation in the final catalog (blue squares), and earthquakes detected per day, from the initial catalog (red) and the final catalog (black). (d) Temporal b -value estimates using both the classical maximum likelihood method (black) and the b -more-incomplete method (red). Shaded areas indicate the corresponding uncertainty ranges.

497 the beginning of the sequence and are mostly related to the Pichilemu area, which further
 498 enhances the contrast in detection rates between space and time. As shown in Figure 7c,
 499 the magnitude distribution over time highlights a strong concentration of events around
 500 M_w 2. The earthquake detection rates (Figure 7c) display the expected decay over time,
 501 with occasional swarms that coincide with short-term increases in station availability and
 502 temporary reactivation of the local seismic network. This underlines the strong impact of
 503 station coverage on inferred detection rates, location quality, and the applicability of tem-
 504 plate matching. It also highlights the importance of having well-located events, since there
 505 are periods where template matching could not be applied because of the lack of reliable
 506 reference locations, which produces a heterogeneous spatial distribution of new template
 507 detections.

508 We compute the b -value using two different methods, as illustrated in Figure 7d. For
 509 this analysis, we use batches of 5,000 earthquakes to estimate the b -value as a function of

510 time. Tests with 3,000 and 7,000 event windows give similar long-term trends, and 5,000
 511 events offer a good compromise between temporal resolution and stability. The black line
 512 represents the b -values obtained with the classical maximum likelihood method for events
 513 above M_c , while the red line corresponds to estimates from the b -more-incomplete method
 514 (Lippiello & Petrillo, 2024). At the beginning of the sequence, the classical b -values fluctuate
 515 between about 0.6 and 1.2, before increasing sharply to approximately 1.6 around day 120,
 516 and later fluctuate around 1.2 before tending toward a stable value close to 1.0 at the
 517 end of the period. The early values are characteristically low for an aftershock sequence,
 518 which likely reflects the limited station coverage and the resulting loss of small events in the
 519 catalog. In contrast, the b -more-incomplete method remains much more stable over time,
 520 with values mostly between 1.2 and 1.6 during the first part of the sequence and converging
 521 toward a value close to 1.0 near the end.

522 Values of b above 1 indicate a relative predominance of smaller earthquakes over larger
 523 ones, which is typical for aftershock sequences. The fact that the b -more-incomplete method
 524 can be applied to more incomplete catalogs and relies on magnitude increments rather than
 525 strict completeness makes it less sensitive to station-dependent variations in detectability.
 526 As a result, it provides a more robust description of the temporal evolution of b in this
 527 sequence and reduces the impact of changes in station availability on the inferred stress
 528 state.

529 5 Discussion

530 5.1 Workflow Performance and Limitations

531 In this study, we employ the BPMF automated detection and location workflow (Beaucé
 532 et al., 2024) to build a dense and internally consistent catalog of the Maule aftershock se-
 533 quence. The workflow performs well across most of the study area, although its effectiveness
 534 depends primarily on daily station coverage, which remains the main limitation of the IMAD
 535 network. PhaseNet produced on average between 6,000 and 12,000 P picks per day (max-
 536 imum approximately 24,000), and a similar number of S picks, even though the number
 537 of available stations changed strongly over time. Nevertheless, the picking performance de-
 538 creases for distant offshore events where S-P times exceed 30 s. The sparse and time-variable
 539 network further limits detection consistency, especially during periods of strong data gaps.

540 Within the BPMF workflow, detections rely on the coherence of PhaseNet P- and S-
 541 phase probability time series across stations rather than on the performance of individual
 542 stations. A real earthquake produces coherent increases in phase-arrival probability at
 543 consistent moveouts, so even low individual probabilities sum constructively and generate
 544 a clear CNR peak. This makes the detector sensitive to low-amplitude events without
 545 requiring station-specific thresholds.

546 Because the Maule network is sparse and highly variable in time, the amplitude of the
 547 CNR fluctuates strongly across days. In such conditions, a fixed detection threshold, as
 548 used in more stable networks (Beaucé et al., 2019, 2022), would either miss many events
 549 on quiet days or generate too many false detections when noise levels are high. Instead, we
 550 use a day-dependent threshold based on a high percentile of the daily CNR distribution,
 551 typically the 97th percentile (see Section 4.1). This percentile-based threshold keeps the
 552 detection performance more consistent through the 10-month sequence, at the cost of losing
 553 the smallest events on the quietest or noisiest days.

554 Location accuracy benefits from the regional 3D velocity model (Potin et al., 2025),
 555 which improves the coherence of clusters in the central and northern parts of the domain,
 556 including the Pichilemu region. The improvement is clear in map view and in cross sections
 557 (see, for example, Figure S10 in the Supporting Information), where previously diffuse
 558 clouds align into narrower structures. However, certain areas remain less well constrained.
 559 Offshore events in the outer rise zone and events south of 37 °S are affected by reduced station

560 coverage and lower resolution in the velocity model. These locations should be interpreted
 561 with caution. Overall, the workflow performs well for a sparse and heterogeneous network,
 562 but it does not replace the benefits of a dense permanent array.

563 The matched filter search is stable in this region. Some station–template correlations
 564 can be low (0.2–0.3), but averaging across at least five stations and six channels and apply-
 565 ing an RMS criterion yields robust detections even when individual traces are noisy. This
 566 strategy is widely used in BPF applications (Beaucé et al., 2019, 2022, 2024) and behaves
 567 similarly in the Maule dataset. Matched filtering densifies the catalog and lowers the mag-
 568 nitude of completeness, but newly detected events inherit the location of their template.
 569 These detections refine the temporal sampling and magnitude range of the sequence rather
 570 than the spatial resolution of the catalog. The GPU implementation of BPF makes the
 571 backprojection and template matching stages fast and scalable.

572 Our regional M_L calibration reproduces the reference magnitudes with small bias but
 573 still leaves some residual variability. The residuals, shown in Figure S8 in Supporting In-
 574 formation, defined as $M_{\text{ref}} - M_{\text{pred}}$ for each event, are centered near zero and most values
 575 lie between about -0.5 and 0.5 magnitude units over distances from 10 to 250 km, with
 576 only a few outliers reaching larger absolute values. There is no strong systematic drift with
 577 distance, although a mild trend remains at the smallest magnitudes. This suggests that the
 578 calibration captures the main attenuation pattern and that the remaining scatter is domi-
 579 nated by unresolved path and site effects, together with measurement noise. When residuals
 580 are averaged over several stations per event, they translate into typical M_L uncertainties
 581 of about 0.2–0.3 magnitude units. A more detailed study of frequency-dependent Q , κ ,
 582 and site amplification, using a generalized inversion technique (GIT) to separate source,
 583 path, and site contributions on the same dataset, could further reduce this scatter, but this
 584 is beyond the scope of the present work. Despite this scatter, the calibrated M_L scale is
 585 internally consistent and stabilizes the Mw– M_L relation in the magnitude range most rel-
 586 evant for our aftershock statistics. This internal coherence is what matters for estimating
 587 b -values, mapping spatial variations in seismicity, and comparing the behavior of the crust
 588 and the subducting slab. As shown by recent studies (e.g., Abercrombie & Baltay, 2025;
 589 Abercrombie et al., 2025; Cochran et al., 2025), the seismic moment M_0 is generally better
 590 constrained than f_c , which remains sensitive to the usable frequency range, SNR, and the
 591 spectral fitting models used, especially for low-magnitude events. Here, we use a noise-
 592 weighted, multi-station stack and a percentile-based estimate of the low-frequency plateau
 593 to reduce the influence of noise-dominated frequency bands and improve the robustness of
 594 the spectral estimates. Residual uncertainty remains, however, and we interpret M_0 and f_c
 595 accordingly.

596 5.2 Comparison with Previous Catalogs

597 This aftershock sequence has been the focus of previous studies, resulting in the de-
 598 velopment of other earthquake catalogs. For instance, Lange et al. (2012) used automatic
 599 picking methods to compile a catalog of over 20,000 events spanning the first six months
 600 of the sequence. Similarly, Rietbrock et al. (2012) applied the STA/LTA triggering method
 601 with 2D velocity models, detecting and locating approximately 40,000 earthquakes. While
 602 most of their detailed analyses focused on roughly the first two months after the mainshock,
 603 the published catalog spans nearly 300 days of seismicity. Additionally, Ryder et al. (2012)
 604 produced a catalog using comparable methods, although limited to a shorter period of two
 605 and a half months. All these works provided the foundation for our current understanding
 606 of the Maule aftershock sequence and were produced with the methods available at the
 607 time. They all rely on the same mobile seismic network (IMAD) used in this study. We
 608 revisit the same dataset using modern detection and relocation techniques, with the goal
 609 of extending the magnitude range, improving location accuracy, and resolving small-scale
 610 structures within the Maule rupture zone.

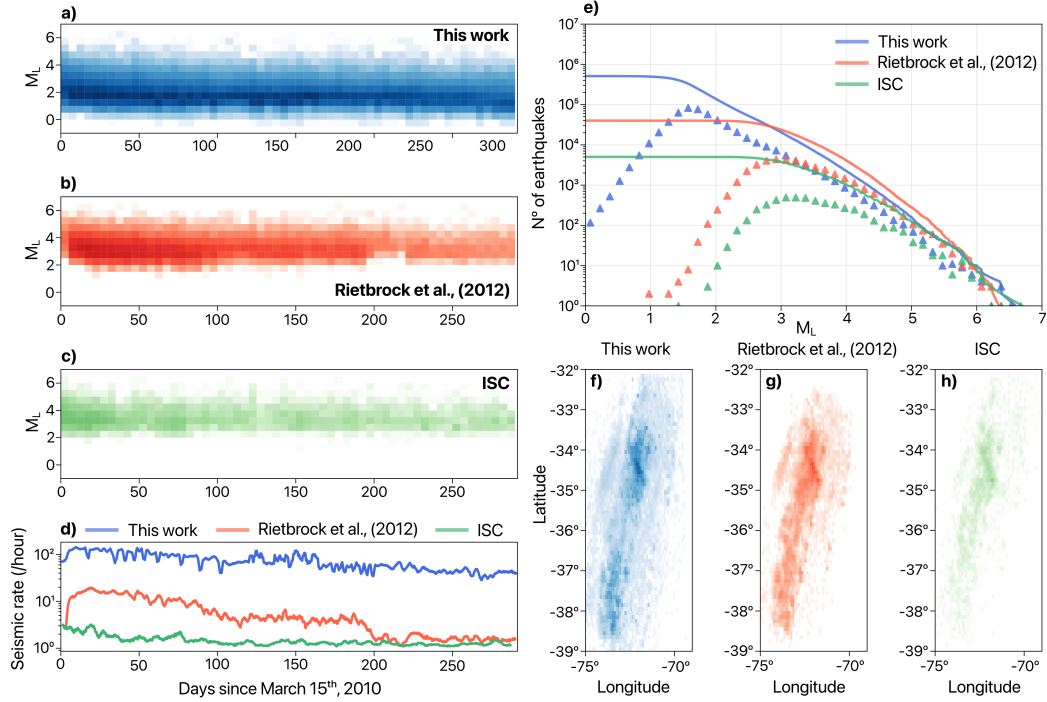


Figure 8. Comparison of three earthquake catalogs based on magnitude distribution, temporal evolution, and spatial coverage for the same period. (a), (b), and (c): 2D histograms showing the distribution of local magnitudes (M_L) over time with bins of 5 days and 0.5 in magnitude. Blue represents the catalog presented in this study, red corresponds to the catalog by Rietbrock et al. (2012), and green denotes the catalog from the ISC (Di Giacomo et al., 2018). Lighter tones indicate lower data density, while darker tones represent higher densities. (d): Seismicity rate (events per hour) over time for the three catalogs, following the same color coding. (e): Magnitude-frequency distribution for the three catalogs. Solid lines represent the cumulative number of events following the Gutenberg–Richter law, while triangles indicate the number of earthquakes for each magnitude bin. (f), (g), and (h): Spatial distribution of seismicity in the rupture zone for each catalog.

611 These catalogs have served as the basis for numerous subsequent studies, including the
 612 characterization of afterslip seismic patterns (Agurto et al., 2012) and the development of
 613 velocity models through local earthquake tomography, which have revealed new structural
 614 features in this segment of the subduction zone (Hicks et al., 2014). Major structures
 615 associated with the Maule earthquake rupture, such as those linked to the subduction slab
 616 and the crustal portion with high seismic activity near Pichilemu, are well represented in
 617 these catalogs (e.g., Ryder et al., 2012) and are consistent in the seismicity distribution.
 618 However, the resolution of fine-scale seismic structures has remained limited.

619 Figure 8 compares the magnitude distribution, temporal evolution, and spatial coverage of
 620 seismicity in three catalogs: Rietbrock et al. (2012), the International Seismic Catalog
 621 (ISC) (Di Giacomo et al., 2018), and ours, for the same time period. While all catalogs
 622 achieve consistent detection completeness for $M_L \geq 3$, our catalog captures a significantly
 623 higher number of small-magnitude events ($M_L \leq 2$). This improvement is especially clear
 624 during periods of low station coverage, when the adaptive threshold and matched-filter
 625 detections maintain stable performance. Our workflow detects 130,575 initial earthquakes
 626 and 537,387 total events after template matching, compared with 40,087 events in the catalog
 627 of Rietbrock et al. (2012) and 5,261 events in the ISC catalog (Di Giacomo et al., 2018). This

628 increase reflects the combined effect of improved phase picking and template-based matched
 629 filtering. The magnitude of completeness also improves from $M_c \approx 2.7$ in Rietbrock et al.
 630 (2012) and above 3.5 in ISC to $M_c \approx 1.8$ in our catalog, which roughly corresponds to an
 631 order of magnitude increase in the number of detected small events.

632 The seismicity rate, as shown in Figure 8d, highlights similar temporal trends across
 633 the three catalogs, but with clear differences in the total number of recorded events. In all
 634 three catalogs, short-term drops in rate follow larger earthquakes, when coda waves mask
 635 smaller aftershocks. These systematic gaps underscore the need to account for detection
 636 limits when interpreting aftershock productivity.

637 The frequency–magnitude distribution of our catalog, compared to the catalogs of
 638 Rietbrock et al. (2012) and the ISC, is presented in Figure 8e. This comparison highlights
 639 the improved detection capability of the proposed workflow, which lowers the magnitude of
 640 completeness by about 1 relative to Rietbrock et al. (2012) and by more than 1.5 relative to
 641 the ISC catalog (Di Giacomo et al., 2018). Differences in the number of moderate-magnitude
 642 events also reflect the fact that each catalog relies on a distinct local–magnitude scale. The
 643 Rietbrock et al. (2012) catalog uses a different M_L formulation based on the methods avail-
 644 able at the time, while our study recalibrates a regional attenuation model directly from
 645 the Maule dataset. Because the ISC catalog relies on a low-density permanent network, it
 646 detects fewer events across all magnitude ranges.

647 Figure 8f–h show that the overall shape of the seismicity distribution is consistent be-
 648 tween catalogs, with a pronounced concentration around the Pichilemu region. Overall, our
 649 catalog reveals additional small-scale structures and secondary clusters, particularly in the
 650 Pichilemu fault area and in the central part of the rupture. In Pichilemu, aftershocks cluster
 651 more tightly along narrow NNW-striking structures and secondary NE-trending branches
 652 than in previous Maule catalogs. In Figure S10, we compare our locations with those of
 653 Rietbrock et al. (2012) using identical map views and cross sections. The tighter clusters
 654 and improved spatial coherence highlight the gains from combining increased completeness
 655 with a 3D velocity model and successive relocation stages (see Text S1 and Figure S10 in
 656 the Supporting Information). This improved resolution, together with the regional M_L cal-
 657 ibration, allows us to map spatial and temporal b -value variations that were not resolved in
 658 earlier work. These improvements are most robust in regions with dense station coverage
 659 and good velocity control, whereas offshore and southern areas remain less well constrained
 660 and should be interpreted carefully.

661 We successfully re-detect approximately 88% of the events reported by Rietbrock et al.
 662 (2012) and 90% of those cataloged by the Centro Nacional de Sismología de Chile (CSN)
 663 and the ISC (Di Giacomo et al., 2018). Events not recovered usually correspond to signals
 664 with too few picks to meet the internal consistency criteria of our workflow. Excluding them
 665 keeps the catalog homogeneous and avoids introducing poorly constrained detections.

666 5.3 Geotectonic Implications

667 This catalog provides a detailed and consistent view of the aftershock sequence of
 668 the 2010 Maule earthquake and shows how different structural domains responded to the
 669 mainshock. The most intense postseismic activity occurs in the Pichilemu area (Figure 9B-B'
 670 and Figure 10), where a shallow normal fault system accommodates upper crustal extension
 671 above the main slip patch. The normal-faulting nature of this system and its potential
 672 reactivation within the area of highest coseismic slip have been well documented (Farías et
 673 al., 2011; Lange et al., 2012; Ryder et al., 2012; Lieser et al., 2014). Using the increased
 674 number of small earthquakes, we refine the view of the Pichilemu fault system in Figure 10.
 675 Seismicity related to this fault system was isolated using HDBSCAN, a hierarchical density-
 676 based algorithm (Campello et al., 2013), often used to distinguish earthquake patterns
 677 within catalogs (Essing & Poli, 2024). The clustering was applied in four dimensions, three
 678 spatial coordinates (latitude, longitude, depth) and origin time.

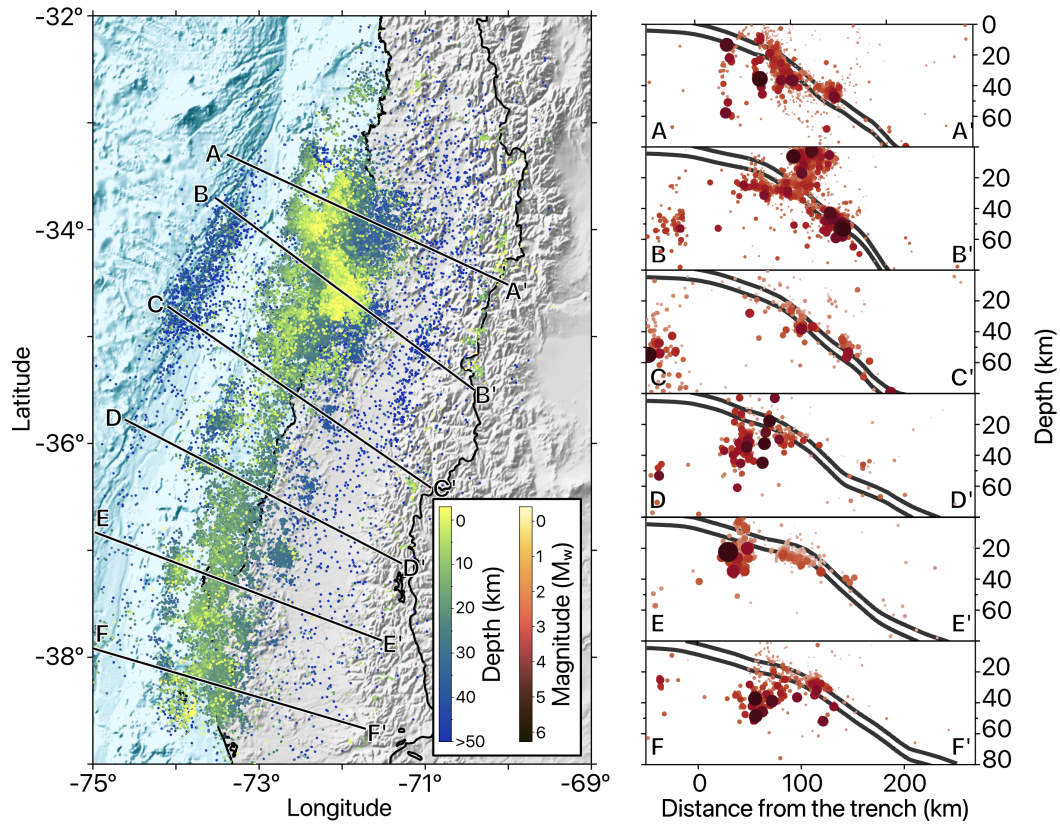


Figure 9. Spatial distribution of seismicity (colored dots) and profiles perpendicular to the subduction trench (black lines, A-F). In the left panel, color represents depth, and in the cross-sections on the right, color indicates magnitude. Black lines in the cross-sections correspond to the slab model (Slab 2.0, Hayes et al., 2018) for the subduction zone in this region.

679 In this area, we observe a main normal fault characterized by an azimuth–dip orientation
680 of $N40^{\circ}W/S30^{\circ}W$ and extending approximately 49 km (Figure 10, A–A’). The fault system
681 shows distinct seismic patterns, with branches approximately perpendicular to the main
682 structure and forming an L-shaped distribution. Seismicity is concentrated between 5 and
683 20 km depth along these intersecting faults, outlining a distributed deformation field around
684 the main fault.

685 This configuration is consistent with a conjugate normal-fault system, where secondary
686 NE–SW structures intersect the main NW–SE fault. The geometry is typical of upper-plate
687 extensional regimes along the Chilean margin (e.g., J. A. Ruiz et al., 2014; Piquer et al.,
688 2019; Santibáñez et al., 2019) and is consistent with seismological models of the largest 2010
689 M_w 6.9 and M_w 7.0 aftershocks in the area (J. A. Ruiz et al., 2014). Comparable conjugate
690 fault patterns have been described in other complex normal-faulting sequences, such as the
691 M_w 6.5 Ludian earthquake (Li et al., 2024) and the M_w 7.1 Ridgecrest earthquake (Liu et
692 al., 2019), supporting an interpretation in terms of localized crustal stretching and stress
693 transfer within the upper plate. Altogether, the seismicity distribution offers a coherent
694 and high-resolution seismological image of the Pichilemu fault system and provides new
695 constraints on its geometry and on the mechanisms of upper-plate fault reactivation in
696 central Chile.

697 Offshore Pichilemu, we also observe clear seismic activity in the outer-rise zone. This
698 finding aligns with previous studies, which suggest that this seismicity is a direct response
699 to the high coseismic slip in the region, potentially resulting from the activation of shallow
700 normal fault systems under extensional forces following large slip events (E. I. Moscoso &
701 Contreras-Reyes, 2012; Lange et al., 2012; Rietbrock et al., 2012; J. A. Ruiz & Contreras-
702 Reyes, 2015). Several events appear near or below 30 km depth. These depth estimates
703 should be interpreted with caution because long travel paths and possible mixing between
704 direct and reflected phases can affect depth estimates in this offshore region.

705 Seismic activity associated with the subducting slab is present throughout the rup-
706 ture zone. Notably, two distinct bands of seismicity are observed along the profiles: one
707 at depths of 20 km to 35 km (Figure 9, A–F) and another, deeper band at approximately
708 50 km, primarily in Figure 9, A–C. A horizontal gap in seismicity is evident in the region
709 closest to the mainshock (Figure 5), suggesting minimal post-mainshock activity in this
710 area, likely due to significant coseismic stress release. In Figure 9, D–F, a spatially coher-
711 ent concentration of events is observed at 30 km to 40 km depth and approximately 50 km
712 landward of the trench. This location lies within the forearc domain where the transition
713 from the frontal accretionary prism to the paleo-accretionary complex marks the onset of
714 seismogenic behavior along the Maule margin (E. Moscoso et al., 2011; Lange et al., 2012).
715 Similar patterns are visible in previously published catalogs (Rietbrock et al., 2012; Lange
716 et al., 2012), indicating that this feature is unlikely to be solely a location artifact. Although
717 reduced model resolution at these latitudes (see Figure S1 in the Supporting Information)
718 limits a detailed interpretation of its geometry, its recurrence across independent datasets
719 is consistent with localized structural heterogeneity in this part of the margin.

720 A marked decrease in aftershock activity is observed around $36^{\circ}S$, near the mainshock
721 hypocenter, defining a distinct low-seismicity zone within the rupture area (Figures 5 and
722 9). South of this region, toward Concepción, the sequence shows sparse and discontinuous
723 seismicity, with small clusters separated by aseismic patches (Figure 9). This quiescence
724 is consistent with substantial coseismic stress release and a limited postseismic response in
725 the southern segment. The scarcity of shallow or interface events emphasizes the along-
726 strike segmentation of deformation and the heterogeneous reactivation of the plate interface
727 following the Maule earthquake. Overall, these patterns outline how the crustal faulting
728 system, the outer-rise region, and the slab responded to stress redistribution after the Maule
729 earthquake.

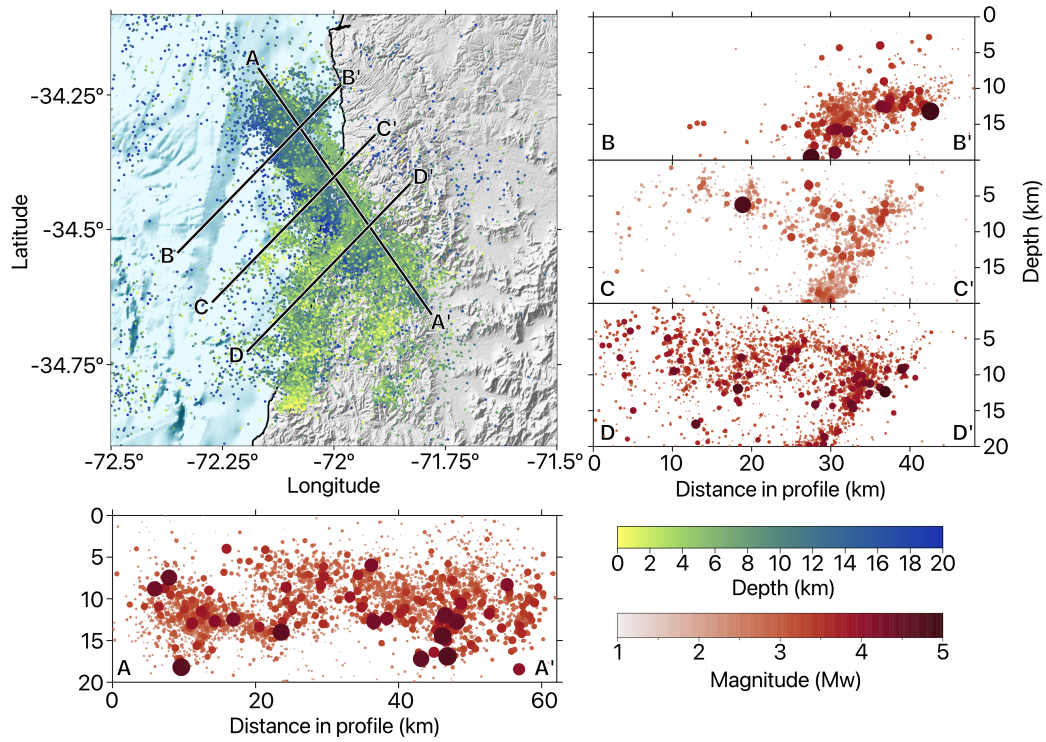


Figure 10. Spatial evolution of the Pichilemu fault system. Earthquakes are shown as dots color-coded by depth in the latitude-longitude map, and by the estimated moment magnitude (M_w) in the cross-sections. Profiles along the black lines (A-D) include one in the main Pichilemu fault's azimuthal direction (A-A') and three perpendicular sections (B-D). The cross-sections illustrate the southwest dip direction of the northwest-trending fault and a series of conjugate faults, forming an L-shaped faulting system.

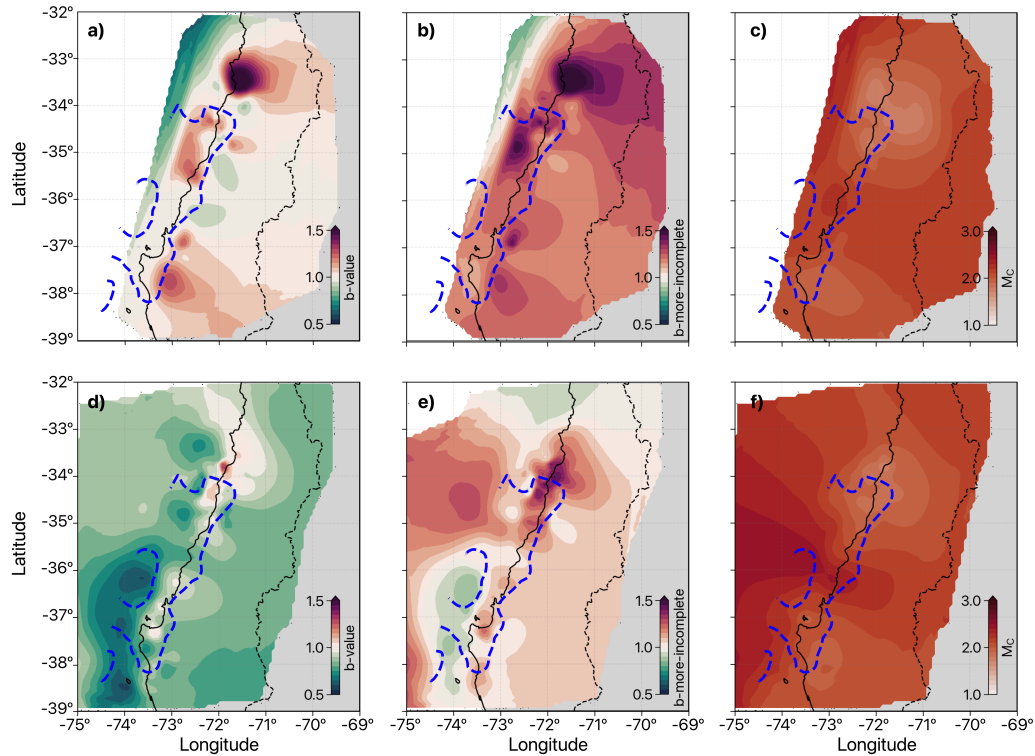


Figure 11. Spatial distribution of the b -value and M_c . We compute these values within earthquake clusters of at least 200 events. (a–c) Crustal seismicity. (d–f) Slab-related seismicity. Columns show the classical b -value, the b -more-incomplete estimate, and the corresponding M_c . The dashed blue line marks the 5 m coseismic slip contour from the model of Yue et al. (2014); regions inside the contour correspond to slip values exceeding 5 m. Values are averages over 100 random k-means clustering iterations, and clusters with fewer than 200 events are discarded.

730

5.4 Spatial Patterns of Seismicity and b -Value Variations

731

732

733

734

735

736

737

738

739

740

741

742

743

744

The b -value provides a simple way to characterize how stress and structure vary across the rupture zone and is linked to fault coupling, stress regime, and fluid content (Custódio & Archuleta, 2006; Chiba, 2019; Folesky, 2024; Collettini & Tinti, 2025). We estimate it using two approaches, the classical maximum likelihood method (Aki, 1965) and the b -more-incomplete method (Lippiello & Petrillo, 2024), which reduces the impact of time-variable completeness. The classical estimate starts with unusually low values (0.6–1.2) during the first weeks, rises sharply to ≈ 1.6 around day 120, and then stabilizes near 1.0 toward the end of the period (Figure 7d). In contrast, the b -more-incomplete remains much more stable, mostly between 1.2 and 1.6 during the first months, and gradually converges toward a value close to 1.0. These differences are closely linked to the evolution of station availability. As shown in Figure 7a, the number of IMAD stations decreases from more than 80 at the start to about 15 at the end of the study period, which affects detectability. As a result, the classical method drops to 0.6–0.8, while the b -more-incomplete remains stable at 1.2–1.6, as it is less sensitive to short-term aftershock incompleteness and variable detection thresholds.

745

746

747

748

To map spatial variations (Figure 11), we follow an iterative clustering strategy (Hartigan, 1975). For each of the $N = 100$ iterations, we randomly select a number of clusters k between 50 and 500, which are then computed using mini-batch k-means (Sculley, 2010; J. Wu, 2012). This produces clusters of variable size, with a typical target of about 400 events per

749 cluster. Clusters with fewer than 200 events are discarded to ensure stable statistics. For
 750 every iteration, we estimate M_c , the classical b -value (Aki, 1965), and the b -more-incomplete
 751 method (Lippiello & Petrillo, 2024) within each remaining cluster, and assign these values to
 752 all earthquakes in that iteration. This process is repeated across all 100 iterations. The final
 753 maps represent the average of all 100 iterations, which smooths out random cluster bound-
 754 aries and yields stable spatial patterns. We avoid interpreting clusters for which M_c is high,
 755 since these areas are more sensitive to detection biases. Given the magnitude uncertainties
 756 and the finite number of events per cluster, we do not treat b -value differences smaller than
 757 about 0.2 as significant and focus instead on robust, large-scale patterns that are stable
 758 across different window sizes and random cluster realizations. While intrinsic uncertainty in
 759 magnitude estimation could propagate into b , prior studies have shown that errors typically
 760 contribute less to b -value variability than magnitude binning and completeness-threshold
 761 choices (Marzocchi & Sandri, 2003; Marzocchi et al., 2020). The gridded fields are obtained
 762 by interpolating the averaged cluster values onto a regular latitude–longitude grid.

763 Figure 11 illustrates the spatial variability of the b -value and the corresponding mag-
 764 nitude of completeness M_c for crustal (a–c) and slab-related (d–f) seismicity. For crustal
 765 events, the classical b -value map (Figure 11a) shows values close to 1.0 along most of the
 766 rupture, increasing to about 1.3 around Pichilemu and in parts of the southern segment.
 767 Values exceed 1.5 in the northern onshore area, where anthropogenic sources (e.g., copper
 768 mining) and numerous small, shallow events are present. We therefore interpret much of
 769 this high- b patch as non-tectonic in origin. The b -more-incomplete estimates (Figure 11b)
 770 retain the first-order along-strike pattern but appear smoother and less sensitive to local
 771 variations in M_c . The crustal M_c map (Figure 11c) ranges from about 1.5 to 3.0, with
 772 higher values offshore and in areas of sparse station coverage, and correlates strongly with
 773 the spatial variability of the classical b -value. This correlation indicates that part of the
 774 spatial variability in the classical b -value map reflects completeness changes rather than
 775 genuine changes in the magnitude–frequency distribution.

776 For slab-related seismicity, classical b -values (Figure 11d) are generally lower, rang-
 777 ing from 0.5 to 1.0 beneath the southern segment and up to approximately 1.3 beneath
 778 Pichilemu, again following the main patterns in M_c . In contrast, the slab b -more-incomplete
 779 map (Figure 11e) reveals a clearer along-strike segmentation, with higher b -values in the
 780 northern part of the rupture and values close to 1.0 in the south. The slab M_c distribu-
 781 tion (Figure 11f) is similar, with higher values where station coverage is sparse. Together,
 782 these maps indicate that classical b -values are strongly influenced by spatial variations in
 783 M_c , whereas the b -more-incomplete estimates provide a more stable representation of the
 784 underlying crustal and slab segmentation that is less sensitive to completeness variations.

785 These spatially variable and temporally evolving b -values are consistent with the idea
 786 that earthquake magnitude distributions reflect a dynamically evolving stress field and struc-
 787 tural heterogeneity (Herrmann et al., 2022). Taken together, the b -more-incomplete esti-
 788 mates highlight a pronounced along-strike contrast in b -value for crustal earthquakes, with
 789 the highest b -values in the northern segment ($\approx 33^\circ$ to 35° S) and lower b -values in the
 790 southern segment ($\approx 36^\circ$ to 38° S). We interpret this contrast as consistent with a weaker,
 791 fluid-influenced plate interface in the north, where elevated pore fluid pressure (p_f) tends to
 792 reduce the effective normal stress ($\sigma_{\text{eff}} = \sigma_n - p_f$) and to favor a higher proportion of small
 793 to moderate earthquakes (Schorlemmer et al., 2005; Scholz, 2015). In contrast, the lower
 794 b -values in the south are compatible with a relatively drier, more strongly coupled interface
 795 and a less fractured upper plate, characterized by lower pore fluid pressure and persistently
 796 high σ_{eff} . Classical b -value estimates remain more sensitive to spatial variations in M_c ,
 797 whereas the b -more-incomplete estimates provide a more robust view of this segmentation
 798 that is less sensitive to completeness variations.

799 Other factors, such as heterogeneous path and site effects or local variations in magni-
 800 tude uncertainty, may also contribute to the observed patterns. This first-order north–south
 801 contrast is, however, consistent with previous interpretations of fluid-rich versus mechani-

802 cally stronger domains derived from geodetic, structural, and b -value analyses (Tassara et
 803 al., 2016; Arroyo-Solórzano & Linkimer, 2021), and is compatible with scenarios in which
 804 fluids released from the dehydrating Nazca slab accumulate and are redistributed along the
 805 plate interface. The strongest b -value gradients occur adjacent to the regions of highest
 806 coseismic slip (Yue et al., 2014), consistent with stress concentration near the edges of the
 807 main slip patches. Together, these patterns support a segmented view of the Maule rupture
 808 and reflect the redistribution of stress, and possibly pore fluid pressure, after the M_w 8.8
 809 earthquake.

810 6 Conclusions

811 This study presents a high-resolution catalog of the 2010 M_w 8.8 Maule earthquake
 812 aftershock sequence in south-central Chile, covering the period from March 2010 to January
 813 2011. By reanalyzing data from the IMAD seismic network with a workflow that combines a
 814 deep-learning-based detection method with relative relocation and template matching, we
 815 identify 537,387 earthquakes, about 13 times more events than reported in previous studies.
 816 The catalog spans magnitudes from M_w 0.2 to M_w 6.2, reaches a completeness level of about
 817 M_w 1.8, and resolves fine-scale seismic structures along the rupture zone, particularly in the
 818 Pichilemu region.

819 The two estimation methods reveal markedly different temporal evolutions of the b -
 820 value. The b -more-incomplete approach yields consistently high values throughout most of
 821 the sequence, whereas the classical maximum likelihood estimate begins with anomalously
 822 low values and increases over time. Despite these contrasting trends, both methods converge
 823 toward $b \sim 1$ after approximately 270 days. This apparent stabilization may reflect a
 824 progressive transition toward a more stable aftershock regime. However, the concurrent loss
 825 of seismic stations during the later stages makes it difficult to determine whether this trend
 826 reflects a genuine physical process or an artifact of decreasing detection capability.

827 Spatially, the catalog reveals a clear along-strike segmentation of b -values. Higher b -
 828 values in the northern segment and lower values in the southern segment are consistent
 829 with along-strike variations in effective normal stress, $\sigma_{\text{eff}} = \sigma_n - p_f$. Elevated pore-fluid
 830 pressure in the north likely reduces σ_{eff} , promoting a higher proportion of small to moderate
 831 earthquakes, whereas lower b -values in the south are consistent with a relatively fluid-poor,
 832 more strongly coupled plate interface and a less fractured upper plate. Taken together
 833 with previous geodetic and structural studies that document two main high-slip regions and
 834 long-term forearc segmentation along the Maule margin (Moreno et al., 2010; Jara-Munoz
 835 et al., 2015; Tassara et al., 2016), these contrasts suggest that along-strike variations in
 836 stress, fluid pressure, and inherited structure exert a first-order control on the postseismic
 837 evolution of the sequence.

838 This catalog provides a detailed and internally consistent dataset that enables future in-
 839 vestigations of key physical processes governing the rupture potential and dynamic evolution
 840 of seismicity in subduction margins. It offers opportunities to correlate seismic observations
 841 with geodetic models (e.g., afterslip, coupling maps) and to better constrain earthquake
 842 source parameters (e.g., source spectral properties, attenuation, and site effects). Finally,
 843 we demonstrate that this workflow provides a robust framework for studying earthquake
 844 sequences across diverse tectonic settings, even in regions with heterogeneous data coverage
 845 and varying seismic network deployments.

846 Data Availability Statement

847 The complete earthquake catalog is provided both in the Supporting Information and
 848 in the Zenodo repository described by Flores-Allende et al. (2026) (<https://doi.org/10.5281/zenodo.18943991>). The Supporting Information provides complementary material related to the workflow, while the Zenodo repository contains the Python scripts

851 together with detailed instructions on how to reproduce the workflow. Seismic waveform
 852 data were accessed online from the contributing seismic networks, and all records remain
 853 publicly available through their corresponding data centers. The IMAD network (Beck et
 854 al., 2014) includes the FDSN code XS (Vilotte et al., 2011), operated by CNRS-INSU and
 855 IRIS/PASSCAL, with data publicly available at the RESIF data center ([https://doi.org/](https://doi.org/10.15778/RESIF.XS2010)
 856 [10.15778/RESIF.XS2010](https://doi.org/10.15778/RESIF.XS2010)). The FDSN code XY (Steve Roecker & Ray Russo, 2010) was op-
 857 erated by GEF/SeisUK, and its data are accessible through the IRIS data center ([https://](https://www.iris.edu/hq/)
 858 www.iris.edu/hq/). The 3A network, also operated by GEF/SeisUK, is available via IRIS.
 859 The ZE network, provided by GIPP (GFZ), can be accessed through the GEOFON data cen-
 860 ter (<https://geofon.gfz.de/waveform/archive/network.php?ncode=ZE&year=2010>).

861 All algorithms used in this study are open source and publicly available. The Back-
 862 Projection and Matched-Filtering (BPMF) workflow (Beaucé et al., 2024) is accessible
 863 at https://github.com/ebeauce/Seismic_BPMF. The NonLinLoc-SSST-Coherence algo-
 864 rithm (Lomax & Savvaidis, 2022) is available at <http://alomax.free.fr/nlloc/> and
 865 through Zenodo (<https://zenodo.org/records/13693145>). SourceSpec (Satriano, 2021)
 866 can be found at <https://github.com/SeismicSource/sourcespec>, and the implementa-
 867 tion of *b*-value estimation methods (Lippiello & Petrillo, 2024) is provided at [https://](https://github.com/caccioppoli/b$-more-positive)
 868 [github.com/caccioppoli/b\\$-more-positive](https://github.com/caccioppoli/b$-more-positive).

869 All computations were performed using Python version 3.11.11 (Van Rossum et al.,
 870 2007) (<https://www.python.org/>). The main scientific libraries used are ObsPy 1.4.2
 871 (Beyreuther et al., 2010) for waveform retrieval and preprocessing ([https://doi.org/10](https://doi.org/10.5281/zenodo.15309143)
 872 [.5281/zenodo.15309143](https://doi.org/10.5281/zenodo.15309143)); SciPy 1.13.0 (Virtanen et al., 2020) for optimization and interpo-
 873 lation (<https://scipy.org/>); and Scikit-learn 1.6.1 (Pedregosa et al., 2011) for data anal-
 874 ysis, including clustering with HDBSCAN (McInnes et al., 2017) and MiniBatch K-means
 875 (J. Wu, 2012) (<https://scikit-learn.org/stable/>). Figures were created using Mat-
 876 plotlib 3.10.1 (Hunter, 2007) (<https://matplotlib.org/>), and maps were produced with
 877 PyGMT (Wessel et al., 2019; Uieda et al., 2021) ([https://www.genericmapping-tools](https://www.genericmapping-tools.org/)
 878 [.org/](https://www.genericmapping-tools.org/)) and Cartopy 0.24.1 (Met Office, 2015) ([https://scitools.org.uk/cartopy/docs/](https://scitools.org.uk/cartopy/docs/latest/)
 879 [latest/](https://scitools.org.uk/cartopy/docs/latest/)).

880 Conflict of Interest Statement

881 The authors have no conflicts of interest to disclose.

882 Acknowledgments

883
 884 This work was funded through the ANR-22-CPJ1-0020-01 program. E. Beaucé was
 885 funded by the Brinson Foundation. L.F. Bonilla was funded by project ANR E-City,
 886 AAPG 2021 – CES 22. Continuous seismic data were provided thanks to the collabora-
 887 tive efforts of IRIS, IPGP, ENS, and GFZ. Numerical computations were conducted on the
 888 S-CAPAD/DANTE platform at IPGP, France. We sincerely thank Sergio Ruiz and Raúl
 889 Madariaga for their valuable discussions on seismicity in the Maule region. We also acknowl-
 890 edge Javier Ojeda, Leoncio Cabrera, and Martin Vallée for their insightful contributions to
 891 discussions on seismic parameters relevant to this study. Additionally, we extend our appre-
 892 ciation to Antony Lomax, Jannes Münchmeyer, and Bertrand Potin for their constructive
 893 feedback on the event relocation process. We also thank the Andes-FrenSZ collaboration
 894 research program and associated researchers for their valuable comments and contributions.
 895 Finally, we are grateful to all researchers at IPGP, Universidad de Chile, and ISTerre who
 896 provided thoughtful insights, discussions, and feedback that contributed to improving this
 897 study. We are grateful to the journal editor Rachel Abercrombie, the associate editor and
 898 three anonymous reviewers for their constructive comments and suggestions that signifi-
 899 cantly improved the quality and clarity of this work.

References

- 900
- 901 Abercrombie, R. E., Baltay, A., Chu, S., Taira, T., Bindi, D., Boyd, O. S., ... others
 902 (2025). Overview of the scec/usgs community stress drop validation study using the
 903 2019 ridgecrest earthquake sequence. *Bulletin of the Seismological Society of America*,
 904 *115*(3), 734–759.
- 905 Abercrombie, R. E., & Baltay, A. S. (2025). Magnitude, depth, and methodological vari-
 906 ations of spectral stress drop within the scec/usgs community stress drop validation
 907 study using the 2019 ridgecrest earthquake sequence. *Bulletin of the Seismological*
 908 *Society of America*, *115*(6), 2741–2768.
- 909 Agurto, H., Rietbrock, A., Ryder, I., & Miller, M. (2012). Seismic-afterslip characteriza-
 910 tion of the 2010 mw 8.8 maule, chile, earthquake based on moment tensor inversion.
 911 *Geophysical Research Letters*, *39*(20).
- 912 Aki, K. (1965). Maximum likelihood estimate of b in the formula $\log n = a - bm$ and its
 913 confidence limits. *Bull. Earthquake Res. Inst., Tokyo Univ.*, *43*, 237–239.
- 914 Allen, R. (1982). Automatic phase pickers: Their present use and future prospects. *Bulletin*
 915 *of the Seismological Society of America*, *72*(6B), S225–S242.
- 916 Anstey, N. A. (1964). Correlation techniques—a review. *Geophysical Prospecting*, *12*(4),
 917 355–382.
- 918 Aron, F., Cembrano, J., Astudillo, F., Allmendinger, R. W., & Arancibia, G. (2015).
 919 Constructing forearc architecture over megathrust seismic cycles: Geological snapshots
 920 from the maule earthquake region, chile. *Bulletin*, *127*(3-4), 464–479.
- 921 Arroyo-Solórzano, M., & Linkimer, L. (2021). Spatial variability of the b -value and seismic
 922 potential in costa rica. *Tectonophysics*, *814*, 228951.
- 923 Báth, M. (1965). Lateral inhomogeneities of the upper mantle. *Tectonophysics*, *2*(6),
 924 483–514.
- 925 Beaucé, E., Frank, W. B., Paul, A., Campillo, M., & van Der Hilst, R. D. (2019). Systematic
 926 detection of clustered seismicity beneath the southwestern alps. *Journal of Geophysical*
 927 *Research: Solid Earth*, *124*(11), 11531–11548.
- 928 Beaucé, E., Frank, W. B., & Romanenko, A. (2018). Fast matched filter (fmf): An effi-
 929 cient seismic matched-filter search for both cpu and gpu architectures. *Seismological*
 930 *Research Letters*, *89*(1), 165–172.
- 931 Beaucé, E., Frank, W. B., Seydoux, L., Poli, P., Groebner, N., van der Hilst, R. D., &
 932 Campillo, M. (2024). Bpmf: A backprojection and matched-filtering workflow for
 933 automated earthquake detection and location. *Seismological Research Letters*, *95*(2A),
 934 1030–1042. Retrieved from <https://zenodo.org/records/14838292> ([Software])
 935 doi: 10.5281/zenodo.14838292
- 936 Beaucé, E., van der Hilst, R. D., & Campillo, M. (2022). Microseismic constraints on the
 937 mechanical state of the north anatolian fault zone 13 years after the 1999 m7. 4 izmit
 938 earthquake. *Journal of Geophysical Research: Solid Earth*, *127*(9), e2022JB024416.
- 939 Beck, S., Rietbrock, A., Tilmann, F., Barrientos, S., Meltzer, A., Oncken, O., ... Russo,
 940 R. M. (2014). Advancing subduction zone science after a big quake. *Eos, Transactions*
 941 *American Geophysical Union*, *95*(23), 193–194. ([Dataset])
- 942 Beyreuther, M., Barsch, R., Krischer, L., Megies, T., Behr, Y., & Wassermann, J. (2010).
 943 Obspy: A python toolbox for seismology. *Seismological Research Letters*, *81*(3), 530–
 944 533. Retrieved from <https://zenodo.org/records/15309143> ([Software]) doi:
 945 10.5281/zenodo.15309143
- 946 Bilek, S. L., & Lay, T. (2018). Subduction zone megathrust earthquakes. *Geosphere*, *14*(4),
 947 1468–1500.
- 948 Bormann, P. (2012). Magnitude calibration formulas and tables, comments on their use and
 949 complementary data. *New Manual of Seismological Observatory Practice 2 (NMSOP-*
 950 *2)*, 1–19. Retrieved from https://doi.org/10.2312/GFZ.NMSOP-2_DS.3.1 (In: Bor-
 951 mann, P. (Ed.), *New Manual of Seismological Observatory Practice 2 (NMSOP-2)*)
 952 doi: 10.2312/GFZ.NMSOP-2_DS.3.1
- 953 Brune, J. N. (1970). Tectonic stress and the spectra of seismic shear waves from earthquakes.
 954 *Journal of geophysical research*, *75*(26), 4997–5009.

- 955 Cabrera, L., Ruiz, S., Poli, P., Contreras-Reyes, E., Osses, A., & Mancini, R. (2021). North-
 956 ern chile intermediate-depth earthquakes controlled by plate hydration. *Geophysical*
 957 *Journal International*, *226*(1), 78–90.
- 958 Campello, R. J., Moulavi, D., & Sander, J. (2013). Density-based clustering based on
 959 hierarchical density estimates. In *Pacific-asia conference on knowledge discovery and*
 960 *data mining* (pp. 160–172).
- 961 Campos, J., Hatzfeld, D., Madariaga, R., López, G., Kausel, E., Zollo, A., ... Lyon-Caen,
 962 H. (2002). A seismological study of the 1835 seismic gap in south-central chile. *Physics*
 963 *of the Earth and Planetary Interiors*, *132*(1-3), 177–195.
- 964 Chiba, K. (2019). Spatial and temporal distributions of b-values related to long-term slow-
 965 slip and low-frequency earthquakes in the bungo channel and hyuga-nada regions,
 966 japan. *Tectonophysics*, *757*, 1–9.
- 967 Cochran, E. S., Baltay, A., Chu, S., Abercrombie, R. E., Bindi, D., Chen, X., ... Trugman,
 968 D. T. (2025). Sccec/usgs community stress-drop validation study: How spectral fitting
 969 approaches influence measured source parameters. *Bulletin of the Seismological Society*
 970 *of America*, *115*(3), 760–776.
- 971 Collettini, C., & Tinti, E. (2025). The influence of lithology and fault source volume on
 972 the magnitude–frequency-distribution of earthquakes. *Geophysical Research Letters*,
 973 *52*(2), e2024GL110354.
- 974 Condori, C., Tavera, H., Marotta, G. S., Rocha, M. P., & França, G. S. (2017). Calibration
 975 of the local magnitude scale (ml) for peru. *Journal of Seismology*, *21*(4), 987–999.
- 976 Custódio, S., & Archuleta, R. (2006). b-values as a proxy for stress–inferences for dynamic
 977 modeling of the 2004 parkfield earthquake. *EOS Trans. AGU*, *87* (52), *Fall Meet.*
 978 *Suppl., Abstract S23C*, 167.
- 979 Deichmann, N. (2017). Theoretical basis for the observed break in ml/m w scaling between
 980 small and large earthquakes. *Bulletin of the Seismological Society of America*, *107*(2),
 981 505–520.
- 982 Delouis, B., Nocquet, J.-M., & Vallée, M. (2010). Slip distribution of the february 27, 2010
 983 mw= 8.8 maule earthquake, central chile, from static and high-rate gps, insar, and
 984 broadband teleseismic data. *Geophysical Research Letters*, *37*(17).
- 985 Di Giacomo, D., Engdahl, E. R., & Storchak, D. A. (2018). The isc-gem earthquake
 986 catalogue (1904–2014): status after the extension project. *Earth System Science Data*,
 987 *10*(4), 1877–1899.
- 988 Essing, D., & Poli, P. (2024). Unraveling earthquake clusters composing the 2014 alto tibe-
 989 rina earthquake swarm via unsupervised learning. *Journal of Geophysical Research:*
 990 *Solid Earth*, *129*(1), e2022JB026237.
- 991 Farge, G., & Brodsky, E. E. (2025). The big impact of small quakes on tectonic tremor
 992 synchronization. *Science Advances*, *11*(20), eadu7173.
- 993 Farías, M., Comte, D., Roecker, S., Carrizo, D., & Pardo, M. (2011). Crustal extensional
 994 faulting triggered by the 2010 chilean earthquake: The pichilemu seismic sequence.
 995 *Tectonics*, *30*(6).
- 996 Felzer, K. R., Abercrombie, R. E., & Ekstrom, G. (2004). A common origin for aftershocks,
 997 foreshocks, and multiplets. *Bulletin of the Seismological Society of America*, *94*(1),
 998 88–98.
- 999 Flores-Allende, R., Seydoux, L., Beauce, E., Bonilla, L.-F., Guéguen, P., & Satriano, C.
 1000 (2026). *Repository for mw 8.8 maule aftershock deep-learning-based catalog*. Dataset.
 1001 Zenodo. Retrieved from <https://doi.org/10.5281/zenodo.18943991> doi: 10.5281/
 1002 zenodo.18943991
- 1003 Folesky, J. (2024). Different earthquake nucleation conditions revealed by stress drop and
 1004 b-value mapping in the northern chilean subduction zone. *Scientific Reports*, *14*(1),
 1005 12182.
- 1006 Frank, W., & Shapiro, N. (2014). Automatic detection of low-frequency earthquakes (lfes)
 1007 based on a beamformed network response. *Geophysical Journal International*, *197*(2),
 1008 1215–1223.
- 1009 Geffers, G., Main, I., & Naylor, M. (2022). Biases in estimating b-values from small earth-

- 1010 quake catalogues: how high are high b-values? *Geophysical Journal International*,
 1011 229(3), 1840–1855.
- 1012 Gibbons, S. J., & Ringdal, F. (2006). The detection of low magnitude seismic events
 1013 using array-based waveform correlation. *Geophysical Journal International*, 165(1),
 1014 149–166.
- 1015 Glodny, J., Echtler, H., Collao, S., Ardiles, M., Burón, P., & Figueroa, O. (2008). Differential
 1016 late paleozoic active margin evolution in south-central chile (37° s–40° s)—the lanalhue
 1017 fault zone. *Journal of South American Earth Sciences*, 26(4), 397–411.
- 1018 Gutenberg, B., & Richter, C. F. (1944). Frequency of earthquakes in california. *Bulletin of*
 1019 *the Seismological Society of America*, 34(4), 185–188.
- 1020 Guéguen, P., Renault, M., Bourova, E., Péquignat, C., Cougoulat, G., Mariscal, A., ...
 1021 Paul, A. (2011). Chilean aftershock network installed one week after the mw 8.8
 1022 chile earthquake: Preliminary analysis of the accelerometric data. In *Poster* (p. 1).
 1023 Retrieved from <http://bdsis.obs.ujf-grenoble.fr/BDSis/>
- 1024 Haberland, C., Rietbrock, A., Lange, D., Bataille, K., & Dahm, T. (2009). Structure of
 1025 the seismogenic zone of the southcentral chilean margin revealed by local earthquake
 1026 travelttime tomography. *Journal of Geophysical Research: Solid Earth*, 114(B1).
- 1027 Hanks, T. C., & Kanamori, H. (1979). A moment magnitude scale. *Journal of Geophysical*
 1028 *Research: Solid Earth*, 84(B5), 2348–2350.
- 1029 Hartigan, J. A. (1975). *Clustering algorithms*. John Wiley & Sons, Inc.
- 1030 Hayes, G. P., Moore, G. L., Portner, D. E., Hearne, M., Flamme, H., Furtney, M., &
 1031 Smoczyk, G. M. (2018). Slab2, a comprehensive subduction zone geometry model.
 1032 *Science*, 362(6410), 58–61.
- 1033 Herrmann, M., Piegari, E., & Marzocchi, W. (2022). Revealing the spatiotemporal complex-
 1034 ity of the magnitude distribution and b-value during an earthquake sequence. *Nature*
 1035 *Communications*, 13(1), 5087.
- 1036 Hervé, F., Godoy, E., Parada, M. A., Ramos, V., Rapela, C., Mpodozis, C., & Davidson, J.
 1037 (1987). A general view on the chilean-argentine andes, with emphasis on their early
 1038 history. *Circum-Pacific Orogenic Belts and Evolution of the Pacific Ocean Basin*, 18,
 1039 97–113.
- 1040 Hervé, F., Munizaga, F., Parada, M., Brook, M., Pankhurst, R., Snelling, N., & Drake,
 1041 R. (1988). Granitoids of the coast range of central chile: geochronology and geologic
 1042 setting. *Journal of South American Earth Sciences*, 1(2), 185–194.
- 1043 Hicks, S. P., Rietbrock, A., Ryder, I. M., Lee, C.-S., & Miller, M. (2014). Anatomy of
 1044 a megathrust: The 2010 mw 8.8 maule, chile earthquake rupture zone imaged using
 1045 seismic tomography. *Earth and Planetary Science Letters*, 405, 142–155.
- 1046 Hunter, J. D. (2007). Matplotlib: A 2d graphics environment. *Computing in Science &*
 1047 *Engineering*, 9(3), 90–95. Retrieved from <https://zenodo.org/records/15375714>
 1048 ([Software]) doi: 10.5281/zenodo.15375714
- 1049 Jara-Munoz, J., Melnick, D., Brill, D., & Strecker, M. R. (2015). Segmentation of the 2010
 1050 maule chile earthquake rupture from a joint analysis of uplifted marine terraces and
 1051 seismic-cycle deformation patterns. *Quaternary Science Reviews*, 113, 171–192.
- 1052 Jara-Muñoz, J., Melnick, D., Li, S., Socquet, A., Cortés-Aranda, J., Brill, D., & Strecker,
 1053 M. (2022). The cryptic seismic potential of the pichilemu blind fault in chile revealed
 1054 by off-fault geomorphology. *Nature Communications*, 13(1), 3371.
- 1055 Lange, D., Tilmann, F., Barrientos, S. E., Contreras-Reyes, E., Methe, P., Moreno, M., ...
 1056 et al. (2012). Aftershock seismicity of the 27 february 2010 mw 8.8 maule earthquake
 1057 rupture zone. *Earth and Planetary Science Letters*, 317, 413–425.
- 1058 Langston, C. A., Brazier, R., Nyblade, A. A., & Owens, T. J. (1998). Local magnitude scale
 1059 and seismicity rate for tanzania, east africa. *Bulletin of the Seismological Society of*
 1060 *America*, 88(3), 712–721.
- 1061 Li, J., Hao, M., & Cui, Z. (2024). A high-resolution aftershock catalog for the 2014 m s
 1062 6.5 ludian (china) earthquake using deep learning methods. *Applied Sciences*, 14(5),
 1063 1997.
- 1064 Lieser, K., Grevemeyer, I., Lange, D., Flueh, E., Tilmann, F., & Contreras-Reyes, E. (2014).

- 1065 Splay fault activity revealed by aftershocks of the 2010 mw 8.8 maule earthquake,
 1066 central chile. *Geology*, *42*(9), 823–826.
- 1067 Lippiello, E., & Petrillo, G. (2024). b-more-incomplete and b-more-positive: Insights
 1068 on a robust estimator of magnitude distribution. *Journal of Geophysical Research:*
 1069 *Solid Earth*, *129*(2), e2023JB027849. Retrieved from [https://zenodo.org/records/](https://zenodo.org/records/8343629)
 1070 [8343629](https://zenodo.org/records/8343629) ([Software]) doi: 10.5281/zenodo.8343629
- 1071 Liu, C., Lay, T., Brodsky, E. E., Dascher-Cousineau, K., & Xiong, X. (2019). Coseismic
 1072 rupture process of the large 2019 ridgecrest earthquakes from joint inversion of geodetic
 1073 and seismological observations. *Geophysical Research Letters*, *46*(21), 11820–11829.
- 1074 Lomax, A. (2001). *Nonlinloc home page*.
- 1075 Lomax, A., Michelini, A., Curtis, A., & Meyers, R. (2009). Earthquake location, direct,
 1076 global-search methods. *Encyclopedia of complexity and systems science*, *5*, 2449–2473.
- 1077 Lomax, A., & Savvaidis, A. (2022). High-precision earthquake location using source-specific
 1078 station terms and inter-event waveform similarity. *Journal of Geophysical Research:*
 1079 *Solid Earth*, *127*(1), e2021JB023190. Retrieved from [https://zenodo.org/records/](https://zenodo.org/records/13693145)
 1080 [13693145](https://zenodo.org/records/13693145) ([Software]) doi: 10.5281/zenodo.13693145
- 1081 Lorito, S., Romano, F., Atzori, S., Tong, X., Avallone, A., McCloskey, J., . . . Piatanesi, A.
 1082 (2011). Limited overlap between the seismic gap and coseismic slip of the great 2010
 1083 chile earthquake. *Nature Geoscience*, *4*(3), 173–177.
- 1084 Madariaga, R., Métois, M., Vigny, C., & Campos, J. (2010). Central chile finally breaks.
 1085 *Science*, *328*(5975), 181–182.
- 1086 Mancini, S., Segou, M., Werner, M. J., Parsons, T., Beroza, G., & Chiaraluce, L. (2022). On
 1087 the use of high-resolution and deep-learning seismic catalogs for short-term earthquake
 1088 forecasts: Potential benefits and current limitations. *Journal of Geophysical Research:*
 1089 *Solid Earth*, *127*(11), e2022JB025202.
- 1090 Marsan, D. (2005). The role of small earthquakes in redistributing crustal elastic stress.
 1091 *Geophysical Journal International*, *163*(1), 141–151.
- 1092 Marzocchi, W., & Sandri, L. (2003). A review and new insights on the estimation of the
 1093 b-value and its uncertainty. *Annals of geophysics*, *46*(6).
- 1094 Marzocchi, W., Spassiani, I., Stallone, A., & Taroni, M. (2020). How to be fooled searching
 1095 for significant variations of the b-value. *Geophysical Journal International*, *220*(3),
 1096 1845–1856.
- 1097 McInnes, L., Healy, J., Astels, S., & et al. (2017). hdbscan: Hierarchical density based
 1098 clustering. *J. Open Source Softw.*, *2*(11), 205.
- 1099 Melnick, D., Bookhagen, B., Strecker, M. R., & Echtler, H. P. (2009). Segmentation
 1100 of megathrust rupture zones from fore-arc deformation patterns over hundreds to
 1101 millions of years, arauco peninsula, chile. *Journal of Geophysical Research: Solid*
 1102 *Earth*, *114*(B1).
- 1103 Met Office. (2015). Cartopy: A cartographic python library with a matplotlib interface
 1104 [Computer software manual]. Exeter, UK. Retrieved from [https://zenodo.org/](https://zenodo.org/records/13905945)
 1105 [records/13905945](https://zenodo.org/records/13905945) ([Software]) doi: 10.5281/zenodo.13905945
- 1106 Minetto, R., Helmstetter, A., Schwartz, S., Langlais, M., Nomade, J., & Guéguen, P. (2022).
 1107 Analysis of the spatiotemporal evolution of the maurienne swarm (french alps) based
 1108 on earthquake clustering. *Earth and Space Science*, *9*(7), e2021EA002097.
- 1109 Moreno, M., Rosenau, M., & Oncken, O. (2010). 2010 maule earthquake slip correlates with
 1110 pre-seismic locking of andean subduction zone. *Nature*, *467*(7312), 198–202.
- 1111 Moscoso, E., Grevemeyer, I., Contreras-Reyes, E., Flueh, E. R., Dzierma, Y., Rabbel, W.,
 1112 & Thorwart, M. (2011). Revealing the deep structure and rupture plane of the 2010
 1113 maule, chile earthquake (mw= 8.8) using wide angle seismic data. *Earth and Planetary*
 1114 *Science Letters*, *307*(1-2), 147–155.
- 1115 Moscoso, E. I., & Contreras-Reyes, E. (2012). Outer rise seismicity related to the maule,
 1116 chile 2010 mega-thrust earthquake and hydration of the incoming oceanic lithosphere.
 1117 *Andean Geology*, *39*(3), 564–572.
- 1118 Mousavi, S. M., & Beroza, G. C. (2023). Machine learning in earthquake seismology. *Annual*
 1119 *Review of Earth and Planetary Sciences*, *51*(1), 105–129.

- 1120 Mpodozis, C., & Ramos, V. (1990). The andes of chile and argentina. *Circum Pacific*
 1121 *Council Publications*, 11, 59–90.
- 1122 Myers, S. C., Simmons, N. A., Johannesson, G., & Matzel, E. (2015). Improved regional and
 1123 teleseismic p-wave travel-time prediction and event location using a global 3d velocity
 1124 model. *Bulletin of the Seismological Society of America*, 105(3), 1642–1660.
- 1125 Neighbors, C., Liao, E., Cochran, E. S., Funning, G., Chung, A., Lawrence, J., ...
 1126 Andrés Sepulveda, H. (2015). Investigation of the high-frequency attenuation parameter,
 1127 kappa, from aftershocks of the 2010 m w 8.8 maule, chile earthquake. *Geophysical*
 1128 *Journal International*, 200(1), 200–215.
- 1129 Ojeda, J., Ruiz, S., del Campo, F., & Carvajal, M. (2020). The 21 may 1960 mw 8.1
 1130 concepción earthquake: A deep megathrust foreshock that started the 1960 central-
 1131 south chilean seismic sequence. *Seismological Research Letters*, 91(3), 1617–1627.
- 1132 Pedregosa, F., Varoquaux, G., Gramfort, A., et al. (2011). Scikit-learn: Machine
 1133 learning in python. *Journal of Machine Learning Research*, 12, 2825–2830. Re-
 1134 trieved from <https://zenodo.org/records/14627164> ([Software]) doi: 10.5281/
 1135 zenodo.14627164
- 1136 Peng, Z., & Zhao, P. (2009). Migration of early aftershocks following the 2004 parkfield
 1137 earthquake. *Nature Geoscience*, 2(12), 877–881.
- 1138 Piquer, J., Yáñez, G., Rivera, O., & Cooke, D. (2019). Long-lived crustal damage zones
 1139 associated with fault intersections in the high andes of central chile. *Andean Geology*.
- 1140 Pollitz, F. F., Brooks, B., Tong, X., Bevis, M. G., Foster, J. H., Bürgmann, R., ... others
 1141 (2011). Coseismic slip distribution of the february 27, 2010 mw 8.8 maule, chile
 1142 earthquake. *Geophysical Research Letters*, 38(9).
- 1143 Potin, B., Ruiz, S., Aden-Antoniow, F., Madariaga, R., & Barrientos, S. (2025). A revised
 1144 chilean seismic catalog from 1982 to mid-2020. *Seismological Research Letters*, 96(1),
 1145 484–498.
- 1146 Richter, C. F. (1935). An instrumental earthquake magnitude scale. *Bulletin of the Seis-*
 1147 *mological Society of America*, 25(1), 1–32.
- 1148 Rietbrock, A., Ryder, I., Hayes, G., Haberland, C., Comte, D., Roecker, S., & Lyon-Caen,
 1149 H. (2012). Aftershock seismicity of the 2010 maule mw= 8.8, chile, earthquake:
 1150 Correlation between co-seismic slip models and aftershock distribution? *Geophysical*
 1151 *Research Letters*, 39(8).
- 1152 Ross, Z. E., Idini, B., Jia, Z., Stephenson, O. L., Zhong, M., Wang, X., ... et al. (2019). Hi-
 1153 erarchical interlocked orthogonal faulting in the 2019 ridgecrest earthquake sequence.
 1154 *Science*, 366(6463), 346–351.
- 1155 Ruegg, J., Rudloff, A., Vigny, C., Madariaga, R., De Chabalier, J., Campos, J., ... Dimitrov,
 1156 D. (2009). Interseismic strain accumulation measured by gps in the seismic gap
 1157 between constitución and concepción in chile. *Physics of the Earth and Planetary*
 1158 *Interiors*, 175(1-2), 78–85.
- 1159 Ruiz, J. A., & Contreras-Reyes, E. (2015). Outer rise seismicity boosted by the maule 2010
 1160 mw 8.8 megathrust earthquake. *Tectonophysics*, 653, 127–139.
- 1161 Ruiz, J. A., Hayes, G. P., Carrizo, D., Kanamori, H., Socquet, A., & Comte, D. (2014).
 1162 Seismological analyses of the 2010 march 11, pichilemu, chile m w 7.0 and m w 6.9
 1163 coastal intraplate earthquakes. *Geophysical Journal International*, 197(1), 414–434.
- 1164 Ruiz, S., Aden-Antoniow, F., Baez, J. C., Otarola, C., Potin, B., del Campo, F., ...
 1165 Bernard, P. (2017). Nucleation phase and dynamic inversion of the mw 6.9 val-
 1166 paraíso 2017 earthquake in central chile. *Geophysical Research Letters*, 44(20),
 1167 10,290-10,297. Retrieved from [https://agupubs.onlinelibrary.wiley.com/doi/](https://agupubs.onlinelibrary.wiley.com/doi/abs/10.1002/2017GL075675)
 1168 [abs/10.1002/2017GL075675](https://doi.org/10.1002/2017GL075675) doi: <https://doi.org/10.1002/2017GL075675>
- 1169 Ruiz, S., & Madariaga, R. (2018). Historical and recent large megathrust earthquakes in
 1170 chile. *Tectonophysics*, 733, 37–56.
- 1171 Ruiz, S., Madariaga, R., Astroza, M., Saragoni, G. R., Lancieri, M., Vigny, C., & Campos,
 1172 J. (2012). Short-period rupture process of the 2010 mw 8.8 maule earthquake in chile.
 1173 *Earthquake Spectra*, 28(1_suppl1), 1–18.
- 1174 Ryder, I., Rietbrock, A., Kelson, K., Bürgmann, R., Floyd, M., Socquet, A., ... Carrizo,

- 1175 D. (2012). Large extensional aftershocks in the continental forearc triggered by the
1176 2010 maule earthquake, chile. *Geophysical Journal International*, *188*(3), 879–890.
- 1177 Salazar, K., & McNutt, M. (2011). Report on the 2010 chilean earthquake and tsunami
1178 response. *Reston, Virginia: US Geological Survey*.
- 1179 Santibáñez, I., Cembrano, J., García-Pérez, T., Costa, C., Yáñez, G., Marquardt, C., ...
1180 González, G. (2019). Crustal faults in the chilean andes: geological constraints and
1181 seismic potential. *Andean Geology*, *46*(1), 32–65.
- 1182 Satriano, C. (2021). Sourcespec—earthquake source parameters from s-wave displacement
1183 spectra. *Zenodo*. Retrieved from <https://zenodo.org/records/6954238> ([Soft-
1184 ware]) doi: 10.5281/zenodo.6954238
- 1185 Scholz, C. H. (2015). On the stress dependence of the earthquake b value. *Geophysical
1186 Research Letters*, *42*(5), 1399–1402.
- 1187 Schorlemmer, D., Wiemer, S., & Wyss, M. (2005). Variations in earthquake-size distribution
1188 across different stress regimes. *Nature*, *437*(7058), 539–542.
- 1189 Sculley, D. (2010). Web-scale k-means clustering. In *Proceedings of the 19th international
1190 conference on world wide web* (pp. 1177–1178).
- 1191 Shelly, D. R., Beroza, G. C., & Ide, S. (2007). Non-volcanic tremor and low-frequency
1192 earthquake swarms. *Nature*, *446*(7133), 305–307.
- 1193 Skoumal, R. J., Brudzinski, M. R., Currie, B. S., & Levy, J. (2014). Optimizing multi-
1194 station earthquake template matching through re-examination of the youngstown,
1195 ohio, sequence. *Earth and Planetary Science Letters*, *405*, 274–280.
- 1196 Steve Roecker, & Ray Russo. (2010). *Ramp response for 2010 chile earthquake*. International
1197 Federation of Digital Seismograph Networks. Retrieved from [https://doi.org/10.
1198 .7914/SN/XY_2010](https://doi.org/10.7914/SN/XY_2010) ([Dataset]) doi: 10.7914/SN/XY_2010
- 1199 Tan, Y. J., Waldhauser, F., Ellsworth, W. L., Zhang, M., Zhu, W., Michele, M., ... Segou,
1200 M. (2021). Machine-learning-based high-resolution earthquake catalog reveals how
1201 complex fault structures were activated during the 2016–2017 central italy sequence.
1202 *The Seismic Record*, *1*(1), 11–19.
- 1203 Tassara, A., Soto, H., Bedford, J., Moreno, M., & Baez, J. C. (2016). Contrasting amount
1204 of fluids along the megathrust ruptured by the 2010 maule earthquake as revealed by
1205 a combined analysis of aftershocks and afterslip. *Tectonophysics*, *671*, 95–109.
- 1206 Trugman, D. T., & Shearer, P. M. (2017). Growclust: A hierarchical clustering algorithm
1207 for relative earthquake relocation, with application to the spanish springs and sheldon,
1208 nevada, earthquake sequences. *Seismological Research Letters*, *88*(2A), 379–391.
- 1209 Uieda, L., et al. (2021). Pygmt: A python interface for the generic mapping tools. *SoftwareX*,
1210 *15*, 100703. Retrieved from <https://zenodo.org/records/4592991> ([Software]) doi:
1211 10.5281/zenodo.4592991
- 1212 van der Elst, N. J. (2021). B-positive: A robust estimator of aftershock magnitude dis-
1213 tribution in transiently incomplete catalogs. *Journal of Geophysical Research: Solid
1214 Earth*, *126*(2), e2020JB021027.
- 1215 Van Rossum, G., et al. (2007). Python programming language. In *Usenix annual technical
1216 conference* (Vol. 41, pp. 1–36). Retrieved from [https://www.python.org/downloads/
1217 release/python-31111/](https://www.python.org/downloads/release/python-31111/) ([Software])
- 1218 Vigny, C., Socquet, A., Peyrat, S., Ruegg, J.-C., Métois, M., Madariaga, R., ... et al.
1219 (2011). The 2010 mw 8.8 maule megathrust earthquake of central chile, monitored by
1220 gps. *Science*, *332*(6036), 1417–1421.
- 1221 Vilotte, J., et al. (2011). Seismic network xs: Chile maule aftershock temporary experiment
1222 (resif-sismob). *RESIF-Réseau Sismologique et géodésique Français*.
- 1223 Virtanen, P., Gommers, R., Oliphant, T. E., et al. (2020). Scipy 1.0: Fundamental al-
1224 gorithms for scientific computing in python. *Nature Methods*, *17*, 261–272. Re-
1225 trieved from <https://zenodo.org/records/10840233> ([Software]) doi: 10.5281/
1226 zenodo.10840233
- 1227 Waldhauser, F. (2001). hypodd—a program to compute double-difference hypocenter loca-
1228 tions (hypodd version 1.0-03/2001). *US Geol. Surv. Open File Rep.*, *01*, 113.
- 1229 Wessel, P., Luis, J., Uieda, L., et al. (2019). The generic mapping tools version 6 [software].

- 1230 *Geochemistry, Geophysics, Geosystems*, 20(11), 5556–5564. Retrieved from [https://](https://zenodo.org/records/3407866)
1231 zenodo.org/records/3407866 ([Software]) doi: 10.5281/zenodo.3407866
- 1232 White, M. C., Fang, H., Nakata, N., & Ben-Zion, Y. (2020). Pykonal: a python package
1233 for solving the eikonal equation in spherical and cartesian coordinates using the fast
1234 marching method. *Seismological Research Letters*, 91(4), 2378–2389.
- 1235 Wu, J. (2012). *Advances in k-means clustering: a data mining thinking*. Springer Science
1236 & Business Media. Retrieved from [https://scikit-learn.org/stable/modules/](https://scikit-learn.org/stable/modules/generated/sklearn.cluster.MinibatchKMeans.html)
1237 [generated/sklearn.cluster.MinibatchKMeans.html](https://scikit-learn.org/stable/modules/generated/sklearn.cluster.MinibatchKMeans.html) ([Software])
- 1238 Wu, Y.-M., Allen, R. M., & Wu, C.-F. (2005). Revised ml determination for crustal
1239 earthquakes in taiwan. *Bulletin of the Seismological Society of America*, 95(6), 2517–
1240 2524.
- 1241 Yao, D., Walter, J. I., Meng, X., Hobbs, T. E., Peng, Z., Newman, A. V., ... Protti,
1242 M. (2017). Detailed spatiotemporal evolution of microseismicity and repeating earth-
1243 quakes following the 2012 mw 7.6 nicoya earthquake. *Journal of Geophysical Research:*
1244 *Solid Earth*, 122(1), 524–542.
- 1245 Yue, H., Lay, T., Rivera, L., An, C., Vigny, C., Tong, X., & Baez Soto, J. C. (2014).
1246 Localized fault slip to the trench in the 2010 maule, chile mw= 8.8 earthquake from
1247 joint inversion of high-rate gps, teleseismic body waves, insar, campaign gps, and
1248 tsunami observations. *Journal of Geophysical Research: Solid Earth*, 119(10), 7786–
1249 7804.
- 1250 Zhu, W., & Beroza, G. C. (2019). Phasenet: a deep-neural-network-based seismic arrival-
1251 time picking method. *Geophysical Journal International*, 216(1), 261–273.